# Debris cover and the thinning of Kennicott Glacier, Alaska: in situ measurements, automated ice cliff delineation and distributed melt estimates

Leif S. Anderson[1,2], William H. Armstrong[1,3], Robert S. Anderson[1], and Pascal Buri[4]

[1]Department of Geological Sciences and Institute of Arctic and Alpine Research, University of Colorado Campus Box 450, Boulder, CO 80309, USA
[2]GFZ German Research Centre for Geosciences, Telegrafenberg, 14473 Potsdam, Germany
[3]Department of Geological and Environmental Sciences, Appalachian State University,033 Rankin Science West, ASU Box 32067, Boone, NC 28608-2067, USA
[4]Geophysical Institute, University of Alaska-Fairbanks, 2156 Koyukuk Drive, Fairbanks, AK 99775, USA

*Correspondence to*: Leif Anderson (leif@gfz-potsdam.de)

**Abstract.** Many glaciers are thinning rapidly beneath debris thick enough to reduce melt rates relative to bare ice. Melt hotspots within otherwise continuous debris cover increase area-averaged melt rates, counteracting the melt suppressing effects of debris. Kennicott Glacier, a large Alaska glacier, is thinning most rapidly, upglacier from its terminus, but under insulating debris cover. We explore the role of debris and ice cliffs in controlling this zone of maximum thinning.

We provide abundant in situ measurements of debris thickness (109), sub-debris melt (74), and ice cliff backwasting (60). We also develop a new, accurate method to automatically delineate ice cliffs using high-resolution panchromatic satellite imagery. We then use empirical relationships, to estimate melt area-averaged melt across the lower 8 kilometers of the glacier.

Ice cliffs cover 11.7% of the debris-covered tongue, the most of any glacier studied to date, which contribute 26% of melt in study area with a mean debris thickness of only 13.7 cm. While the relative importance of ice cliffs to melt increases as debris thickens downglacier, the absolute magnitude of area-averaged melt declines towards the terminus.

The primary control on area-average melt rate across the zone of maximum thinning appears to be debris thickness, but maximum surface melt does not align with the zone of maximum thinning. We therefore suggest that the decline in ice discharge from upglacier is the vital control defining the zone of maximum thinning.

**Keywords:** mass balance; WorldView; backwasting; Østrem's curve, debris-covered glacier

## 1 Introduction

Loose rock (debris) is common on glacier surfaces globally and is especially abundant on glaciers in Alaska (Scherler et al., 2018). Where debris is thicker than a few centimeters it insulates the underlying ice, leading to the reduction of melt rates (Østrem, 1959; we refer to 'thick debris' as any debris that reduces melt rates relative to bare-ice melt rates). Adding to this insulating effect, debris is expanding for many glaciers even as they contract in response to climate warming (e.g., Tielidze et al., 2020). Expanding and thickening debris cover should reduce glacier thinning relative to glaciers without debris. But the melt-suppressing effect of debris is not always apparent the observed thinning patterns of glaciers even when debris is thick and debris coverage is extensive (e.g., Kääb et al., 2012; Gardelle et al., 2013). In High Mountain Asia many debris-covered and debris-free glaciers are thinning at similar rates (e.g., Kääb et al., 2012; Brun et al., 2018). This apparent paradox, in which rapid thinning is occurring under insulating debris cover is known as the 'debris-cover anomaly' (Pellicciotti et al., 2015). It has been documented in both Asia and in the European Alps (Nuimura et al., 2012; Agarwal et al., 2017; Lamsal et al., 2017; Wu et al., 2018; Mölg et al., 2019).

The 'debris-cover anomaly' may in fact be a global phenomena. A close look at previously published glacier thinning patterns from the Wrangell Mountains of southeast Alaska reveals that maximum thinning rates from within single glaciers are similar whether debris is present or not (Figs. 1 and 2; Berthier et al., 2010; Das et al., 2014). This is a compelling

because the Wrangell Mountains occur at 61 to 62 deg. N, a latitude and in a region where the effects of debris on glacier mass balance has received almost no attention.

One of the glaciers within the Wrangell Mountains that is thinning rapidly under debris cover is Kennicott Glacier (Figs. 1 and 2). Greater surface elevation changes are documented from the Kennicott debris-covered tongue than from any portion of the largely debris-free Nabesna Glacier, north of Kennicott Glacier (Fig. 2). Why does the maximum thinning of Kennicott Glacier occur under debris at rates similar to nearby debris-free glaciers? To aid our analysis, we define a zone of maximum thinning or *ZMT* where Kennicott glacier thinned at an average rate greater than 1.2 m $yr^{-1}$ between 1957 and 2004 (Figs. 1 and 2; Das et al., 2014). For Kennicott Glacier, thinning rates this high only occur within 4 kilometers of the terminus and under debris. The *ZMT* occupies a 2-km down-glacier by 3.5-km across-glacier portion of the debris-covered tongue. The *ZMT,* as defined, is consistent with maximum thinning rates between 2000 and 2007 based on lidar profiles (Fig. 2; Das et al., 2014).

The continuity equation for ice is fundamental for understanding how glaciers thin, with or without debris. It can be formulated as:

$$\frac{dH}{dt} = \dot{b} - \frac{dQ}{dx} - \frac{dQ}{dy} \quad , \tag{1}$$

where $H$ is the ice thickness, $t$ is time, $\dot{b}$ is the annual specific mass balance (or loosely ice melt in the ablation zone), $Q$ is the column integrated ice discharge (or loosely ice dynamics; Fig. 3), $x$ is the east-west direction, and $y$ is the north-south direction. Constraining $\dot{b}$ on debris-covered glaciers is particularly difficult due to the presence of ice cliffs, ponds, and streams within debris covers. The annual specific balance in the ablation zone can be sub-divided,

$$\dot{b} = \dot{b}_s + \dot{b}_e + \dot{b}_b \tag{2}$$

where $\dot{b}_s$ is the annual surface ablation, $\dot{b}_e$ is the annual englacial ablation, and $\dot{b}_b$ is the annual basal ablation rate. Surface ablation typically dominates $\dot{b}$ in most non-polar glacial settings. We neglect the effects of $\dot{b}_e$ and $\dot{b}_b$ because their contribution to rapid thinning is likely small and it is not yet possible, to quantify them within and under debris-covered tongues. Building from Eq. (1), $\dot{b}_s$ is negative in the ablation zone, and therefore shifts $\frac{dH}{dt}$ towards negative values, thinning the glacier. In the ablation zone, the sum of $\frac{-dQ}{dx} - \frac{dQ}{dy}$ tends to be positive due to slowing ice flow. This ice emergence velocity counters surface lowering due to melt.

Two common explanations for the debris-cover anomaly follow from Eq. (1), which are not mutually exclusive ( Immerzeel et al., 2014; Vincent et al., 2016; Brun et al., 2018). First, it is possible that melt $\dot{b}$, when averaged over glacier widths is higher than we expect from the melt reducing debris alone, therefore leading to rapid thinning. Ponds and ice cliffs have been documented to locally increase melt rates on debris-covered glaciers by an order of magnitude compared to adjacent melt rates measured from under debris (e.g., Immerzeel et al., 2014). M*elt hotspots* such as ice cliffs, ponds, streams, and thermokarst counter the insulating effects of debris by raising area-averaged melt rates (e.g., Kirkbride, 1993; Sakai et al., 2002; Reid and Brock, 2014; Miles et al., 2018). Conceptually, melt hotspots perturb the area-averaged melt rate from a melt rate solely defined by the insulating effects of debris (lower melt rates) towards a melt rate solely defined by the melt of bare-ice (higher melt rates). The degree to which these hotspots increase area-averaged melt rates, is an area of active debate within the community. Second, increased melting upglacier of the debris leads to glacier thinning an reduced ice flow to debris-covered portions of glaciers. This leads to reduced ice emergence rates and locally amplified thinning (e.g., Nye, 1960; Vincent et al., 2016).

Kennicott Glacier holds exceptional potential for reveling the role of melt hotspots in debris-covered glacier thinning. In the last 8 kilometers of Kennicott Glacier more than 10 thousand ice cliffs are scattered within otherwise continuous debris (Anderson, 2014). If melt hotspots are the sole control on the *location and magnitude* of the zone of maximum thinning or *ZMT* for Kennicott Glacier then we should expect melt rates (averaged across the glacier width) from across Kennicott Glacier to be maximized there. Here, we to address three questions: (1) *What is the surface mass balance across the debris-*

*covered tongue and zone of maximum thinning of Kennicott Glacier during the summer of 2011?* 2) *Do ice cliffs maximize glacier-wide melt in the zone of maximum thinning during the summer of 2011?*

To address these questions, we quantify the role of ice cliffs and sub-debris melt across the debris-covered tongue of Kennicott Glacier during the summer of 2011. We limit our scope to ice cliffs and sub-debris melt, leaving an examination of surface ponds and streams as later contributions. Our analysis is rooted in the collection of abundant in situ data from the glacier surface, including: debris thickness, sub-debris melt rates, and ice cliff backwasting rates. In addition to helping address the questions raised above, these in situ measurements, from this latitude and Alaska, are vital for developing a global perspective on glacier response to climate change as well as the next generation of global glacier models incorporating the effects of debris cover.

To determine the mass balance pattern within the debris-covered tongue, ice cliff extent must be quantified. We therefore present and apply a new method for remotely delineating ice cliffs using high-resolution WorldView 1 orthoimages. We combine our in situ measurements and remotely delineated ice cliffs to quantify surface melt rates in a distributed fashion across the zone of maximum thinning, thereby addressing the questions outlined above.

### 1.1 Study glacier

Kennicott Glacier is a broadly south-southeast facing glacier on the south side of the Wrangell Mountains. The glacier exists across a 4600 m elevation range between 4996 and 400 m a.s.l. (Fig. 1; 387 $km^2$ area). For comparison, Khumbu Glacier, in Nepal, has an area of 26.5 $km^2$ and spans an elevation range of 3950 m from 8850 to about 4900 m a.s.l. (Pfeffer et al., 2014). Kennicott Glacier covers almost 15 times more area than the Khumbu Glacier and our study area, the debris-covered tongue of Kennicott Glacier (24.2 $km^2$ ), is only slightly smaller than Khumbu Glacier itself. The main trunk of Kennicott Glacier is 42 km long and is joined by two primary tributaries, the Root and the Gates Glaciers. Kennicott Glacier has only retreated 600 meters since its maximum Little Ice Age extent in 1860 (Figure 4; Rickman and Rosenkrans, 1997; Das et al., 2014; Larsen et al., 2015).

As of 2015, 20% of Kennicott Glacier was debris-covered. At elevations below the equilibrium-line altitude at about 1500 m a.s.l. (Armstrong et al., 2017), 9 medial moraines are identifiable within the debris-covered tongue. These medial moraines form primarily from the erosion of hillslopes above the glacier and express themselves as stripes on the glacier surface (Anderson, 2000). Above 700 m a.s.l., debris is typically about one clast thick (Anderson, 2014). The medial moraines coalesce in the last 7 km of the glacier where ice cliffs, surface ponds, and streams are scattered within otherwise continuous debris cover (Anderson, 2014).

## 2 Methods

Our methods fit into three broad categories: 1) in situ measurements; 2) automatic ice cliff delineation; and 3) distributed melt rate estimates. In situ measurements were made within the broad study area shown in Figure 1C, which is within 8 kilometers of glacier terminus. Distributed melt estimates on the other hand are made across the delineated medial moraines shown in Figure 4A. In total the distributed melt estimates were made over 24.2 $km^2$ which we consider here to be the 'debris-covered tongue' of the glacier. In situ measurements were all made within the full field campaign duration and study period from 18 June to 16 August 2011. We correct each measured melt rate to represent the full duration of the study period, as described below.

### 2.1 In situ measurements

The presence of ice cliffs, surface lakes, and variations in debris thickness on debris-covered glaciers makes distributed estimates of mass balance difficult. In order to remedy this issue we make abundant in situ measurements of debris thickness, sub-debris melt, and ice cliff backwasting across the glacier tongue from late June to late August 2011. Partly because of the significant effort required to make in situ measurements, mass balance research of debris-covered glaciers has been focused on a few keystone glaciers in the Himalaya (e.g., Lirung, Ngozumpa, and Khumbu Glaciers; Benn et al., 2012; Immerzeel et al., 2014) and European Alps (e.g., Miage and Zmutt Glaciers; Brock et al., 2010; Mölg et al., 2019). Sparse in situ observations, relative to bare-ice glaciers, mean that global projections of glacier change cannot yet robustly incorporate the effects of debris cover. Measurements from debris-covered glaciers in new regions like Alaska are therefore needed. In order for debris-covered glacier mass balance models to be applied regionally, basic debris properties and the meteorology above the debris must also be measured. In addition to the measurements presented in the main text, we also

present on-glacier air temperatures and debris thermal conductivities from the summer of 2011, which we provide as supplementary, supporting material.

### 2.1.1 Debris thickness

We measured debris thicknesses at 109 sites. Debris measurement locations coincide with the sites that we also measured ice cliff backwasting and sub-debris melt (Fig. 4; Supplemental material). We measured thicknesses by digging through the debris to the ice surface (after Zhang et al., 2011). Where debris was thinner than ~10 cm we dug 5 pits and recorded the average debris thickness. While we did not measure debris thickness below 450 m a.s.l., visual inspection from across the proglacial pond suggests that debris exceeded 1 m above some ice cliffs. The mean uncertainty of the debris thickness measurements is ±0.3 cm, with a standard deviation of ±1.8 cm, and a maximum error of ±6.7 cm (Fig. 5). Error estimates were based on repeated measurements, but measurement error is a negligible compared to the changes in debris thickness down and across the glacier.

### 2.1.2 Sub-debris melt

We measured sub-debris melt at 74 locations (Fig. 4). At each site, we removed debris, installed ablation stakes and then replaced the debris (Supplemental Figure 1). We placed stakes in debris up to 40 cm thick. Sub-debris melt ( $\dot{b}_{debris}$ ) was measured by removing the debris and measuring ice surface lowering. The mean uncertainty in the sub-debris melt rates was ± 0.1 cm $d^{-1}$, the standard deviation was 0.05 cm $d^{-1}$, and the maximum error was 0.25 cm $d^{-1}$ for the three ablation states with the shortest measurement period of 8 days. These measurement uncertainties are small compared to the changes in melt rate with debris thickness (Fig. 6).

Because melt measurements were made over different time periods we corrected each measurement to represent the full study period. A degree-day factor for sub-debris melt was therefore calculated for each measurement (see supplemental for the full explanation; Hock, 2003**)**. This has a negligible effect on the curve fits we apply below, and the uncertainty added is well within the uncertainty bounds of the distributed melt estimates. We apply this correction non-the-less for completeness.

### 2.1.3 Ice cliff backwasting

Previous studies have estimated ice cliff backwasting rates as they vary in space using DEM-differencing, models, and in situ measurements. These approaches have shown that 1) ice cliff survivability varies strongly with aspect at lower latitude (Sakai et al., 2002; Buri and Pellicciotti, 2018); 2) ice cliff melt rates are highly sensitive to cliff slope (Reid and Brock, 2014); 3) local topography plays an important role in local ice cliff backwasting rates (Steiner et al., 2015); and 4) ponds allow for the long-term persistence of ice cliffs (e.g., Brun et al., 2016; Miles et al., 2016). On Kennicott Glacier, we take advantage of a rich dataset of in-situ backwasting rates from 60 ice cliffs.

We made repeat horizontal distance measurements between the upper ice cliff edge and a stationary marker (in a moving reference frame; after Han et al., 2010). Ice cliff backwasting rates were extrapolated to the full study period by calculating a degree-day factor for each ice cliff using data from the off-ice meteorological stations (see supplemental for full methods). The mean error of the ice cliff backwasting rates is ±0.5 cm $d^{-1}$ (Fig. 7; Supplemental Figure 9). Maximum error is ±1 cm $d^{-1}$ for 10 cliffs that were measured over the shortest interval (21 days). The standard deviation of errors is ±0.2 cm $d^{-1}$.

## 2.2 Automated ice cliff delineation methods

Ice cliffs are common on debris-covered glacier surfaces and important for the surface mass balance, yet quantifying their extent is difficult. Following Herreid and Pellicciotti (2018), previous efforts to delineate ice cliffs have relied on field mapping (e.g., Steiner et al., 2015) from the manual digitization of remotely-sensed data (Sakai et al., 1998; Han et al., 2010; Thompson et al., 2016; Watson et al., 2017; Han et al., 2010; Thompson et al., 2016; Watson et al., 2017), automatically by object based image analysis locally derived with unmanned aerial vehicles (e.g., Kraaijenbrink et al., 2016) or automatically by principal component analysis using visible near-infrared and shortwave infrared satellite bands (Racoviteanu and Williams, 2012). A new method for the delineation of ice cliffs has also been developed using high-resolution digital elevation models (DEMs) with 5-meter resolution (Herreid and Pellicciotti, 2018). Despite the efforts of projects like the ArcticDEM (Porter et al., 2018), glacier coverage with high resolution DEMs (or high-resolution hyperspectral imagery) is still rarer than coverage with orthoimagery. Here we introduce a new method to delineate ice cliffs using only high-resolution satellite imagery. We use this method to delineate the abundant ice cliffs on the surface of Kennicott Glacier.

We describe an automated algorithm to delineate ice cliffs from optical satellite imagery. We use 0.5 m resolution WorldView (WV) satellite imagery acquired on 13 July 2009 (catalog ID: 1020010008B20800) to delineate ice cliffs across the study area. We use the panchromatic band, which integrates radiance across the visible spectrum and provides the highest spatial resolution. The 2009 WV image was the closest high-resolution image available in time to the 2011 summer field campaign. We used WV stereoimagery from 2013 to produce glacier surface DEMs at 5 m spatial resolution using the Ames Stereo Pipeline (Shean et al., 2016), which we use to represent the glacier surface during the study period.

Our method for detecting ice cliffs relies on the observation that ice cliffs are generally darker than the debris around them. Ice cliffs, when actively melting, are typically coated with a thin, wet debris film, which appears darker than the adjacent, dry debris in panchromatic optical imagery (Fig. 8). In addition, steep ice cliffs are often more shaded than nearby lower-sloped debris-covered surfaces.

The workflow we outline relies on open-source Python packages, which facilitates the method's replication and improvement by other researchers. Our workflow consists of three general steps: 1) processing: stretching the image brightness histogram to a suitable range for our ice cliff detection methods; 2) detection: applying an ice cliff detection method; and 3) post-processing: morphologically filtering of the detected ice cliffs (Fig. 8). We apply a linear histogram stretch uniformly across the image, including both the glacier and surrounding off-ice areas. These steps introduce several processing parameters, which we select using a Monte Carlo optimization method. Below, we first present the processing steps, followed by our parameter optimization procedure.

We use two methods to detect ice cliffs: i) the adaptive binary threshold method (*ABT*; skimage.filters.adpative_threshold tool; e.g., Sauvola and Pietikäinen, 2000); and ii) the Sobel edge delineation method (*SED*; skimage.filters.sobel tool; Richards, 2013). In pre-processing, we use separate saturation stretches (Fig. 5) for each method by applying the exposure function in the scikit-image package (skimage). The different methods perform best with different exposure levels, so we create two separate stretched orthoimages in pre-processing.

The *ABT* approach runs a moving window over the image, calculates the mean brightness value within that window, and then uses a threshold to binarize the image. Because the brightness threshold varies across the image, the *ABT* approach is less sensitive to changes in illumination and debris color than a global threshold.

The *SED* approach estimates spatial gradients in image brightness. The Sobel operator detects high contrasts between light-colored debris and dark-colored ice cliffs. The saturation stretch applied on the orthoimage causes dark ice cliffs to appear as featureless black regions, which the Sobel operator returns as low gradient values. We apply a brightness gradient threshold to isolate ice cliffs.

The last step in our processing process is morphological filtering to remove spurious data. Both delineation methods (*ABT* and *SED*) produce false positives from shaded, over-exposed, or textureless debris cover (*SED* only). The *SED* approach produces many false positives, which generally have a characteristic speckled appearance, and often occur in small, isolated groups. We apply morphological opening (Dougherty, 1992) to remove these isolated, distributed false positives (skimage.morphology.opening; Fig. 8). In addition, the *SED* approach creates false positives in regions that have been over-exposed by the saturation stretch and therefore lack texture. We remove these *SED* false positives by masking pixels with the maximum brightness.

To maximize correct ice cliff identification and minimize false positives we compare our ice cliff estimates to hand-digitized ice cliffs from twelve 90,000 $m^2$ regions. The cumulative area used in the validation dataset was 1.8 $km^2$, approximately 7.4% of the 24.2 $km^2$ study area (Fig. 9). There is some operator subjectivity in delineating ice cliffs from satellite imagery, especially for smaller ice cliffs. To minimize this issue, two different human operators independently delineated ice cliffs. As these independent delineations agreed within 3% in their ice cliff area, we consider operator misidentification to be a negligible source of error.

Seven parameters determine the success of these ice cliff delineation methods: i-ii) the low and high end brightness values used for the saturation stretch; iii-iv) the window size and offset from mean brightness in the *ABT* method, v) the high-end value to use for thresholding in the *SED* method, and; vi-vii) the kernel sizes used in morphological filtering of the *SED* and *ABT* results. To find the best parameter set we use a Monte Carlo approach for multi-objective optimization (Yapo et al., 1998). We ran the ice cliff detection algorithm 2500 times with differing parameter choices. In each iteration, every parameter is randomly selected using uniform probability distributions over that respective parameters range of possible values (Duan et al., 1992). This method allows us to efficiently test performance across a wide range of parameter values and is sensitive to interaction between selected parameters across their ranges. We evaluate algorithm performance by

comparing ice cliff area from the automated routine against the hand-digitized validation dataset. Our optimization simultaneously seeks to maximize true positive ice cliff delineation, while minimizing false positives and false negatives. We manually inspect the top-performing parameter sets, ranked by Euclidean distance from the origin (see Supplementary Figure 14), which defines perfect algorithm performance (Supplemental materials; Reed et al., 2013). We chose image processing parameters slightly off the set with the smallest Euclidean distance to reduce false positives (Supplementary Table 3). We reduce false positives at the expense of true positives because this led to a higher ratio of true positives to false positives, so we are more certain that a given detection is likely to be a real ice cliff.

**2.3 Distributed melt estimates**

In order to produce distributed melt estimates, we extrapolate our in situ measurements across the area of the 9 defined medial moraines in Fig. 4. We use empirical curve fits of debris thickness as it varies with elevation and flow path (i.e., by medial moraine), sub-debris melt as it varies with debris thickness, and ice cliff backwasting uniformly across the medial moraines (Figs. 5-7). These estimates represent the period from 18 June to 16 August 2011.

The summer specific mass balance $\dot{b}_s$ is divided into contributions from sub-debris and ice cliff melt: $\dot{b}_{debris}$ and $\dot{b}_{icecliff}$. Each 0.5 m pixel is designated as debris or ice cliff using the *ABT* ice cliff delineation method. We use the *ABT* method because it consistently performs better than the *SED* method (see Results section). For the best case we apply a bias correction by adding 20% to the ice cliff area in each elevation band based on the consistent underprediction of ice cliffs. Extreme ice cliff areas are represented with ±20% areas from this most likely case.

We extrapolate debris thickness across the study area by applying the elevation dependent curve fits to debris-designated pixels. For the five medial moraines in the center of the glacier (labeled 4 -8 in Figure 4A) in which 69% of debris thickness measurements were made, we apply a sigmoidal curve fit (Fig. 5). Within these five medial moraines, debris thickness $h_{debris}$ varies with elevation $z$ according to:

$$h_{debris} = \frac{a}{\left[1+10^{b(z-c)}\right]} + d \quad , \qquad (3)$$

where $a$, $b$, $c$, and d are fitted parameters derived using Matlab's polyfit function (Table 1). We apply this sigmoidal curve fit because it best matches the pattern of debris thicknesses within these five medial moraines when they are binned in 50 m elevation bands. For other medial moraines with fewer debris thickness measurements we apply linear curve-fits. For the western most medial moraine (# 9 in Fig. 4A), which was difficult to access, we apply uniform debris thicknesses based on a few measurements. We test the importance of the debris thickness applied to medial moraine # 9 in the Supplemental material, the importance of this assumed debris thickness is minor and viable debris thicknesses fit well within the uncertainties explored.

We apply sub-debris melt-debris thickness relationship (or hyper-fit model after Anderson and Anderson, 2016) to all debris-designated pixels. In the model, the relationship between specific sub-debris melt $\dot{b}_{debris}$ and debris thickness is:

$$\dot{b}_{debris} = \dot{b}_{ice} \frac{h_*}{\left(h_{debris} + h_*\right)} \quad , \qquad (4)$$

where $\dot{b}_{ice}$, the bare-ice melt rate measured near the top of the study area, and $h_*$ the characteristic debris thickness have values of 5.87 cm $d^{-1}$ and 8.17 cm respectively (Fig. 6). Sub-debris melt rates under debris $h_*$ thick will be half the value of the bare-ice melt rate. If ice is assumed to be at 0° C, $h_*$ can be estimated from physical inputs and parameters following:

$$h_* = \frac{k\,R}{\left(1-\phi\right)} \quad , \qquad (5)$$

where $k$ and $\varphi$ are the thermal conductivity and porosity of the debris cover and $R$ is the thermal resistance of the debris layer. Here we define $R$ as:

$$R = \frac{\overline{T}_s}{L\rho_{ice}\dot{b}_{ice}} \quad , \qquad (6)$$

where $L$ and $\rho_{ice}$ the latent heat of fusion and density of ice, $\bar{T}_s$ the average debris surface temperature over the period used to estimate $h_*$ and $\dot{b}_{ice}$ is the bare-ice melt rate over the period used to estimate $h_*$. The hyperbolic fit between debris thickness and sub-debris melt assumes that energy is transferred through the debris by conduction. While these debris parameters can be measured, in practice they are difficult to measure across debris-covered glaciers so we use an empirical fit to debris thickness-melt data to constrain $h_*$.

We apply the ice cliff backwasting-elevation relationship to all ice cliff pixels. We ignore ice cliff backwasting variation with orientation, as there is no clear relationship between backwasting rate and orientation in our measurements (Fig. 7). We did not find a consistent difference between backwasting for ice cliffs with and without ponds at their base (Fig. 7) and no clear relationship between backwasting rate and medial moraine is apparent either (Supplementary material). We apply the mean specific horizontal ice cliff retreat across the study area:

$$\dot{b}_{backwasting} = f \quad , \quad (7)$$

where $f$ is the mean backwasting rate 7.1 cm $d^{-1}$ (an elevation-dependent pattern is explored in the supplementary material). Because the backwasting rate is measured horizontally, we apply an average dip relative to the horizontal plane ($\theta$) to estimate the melt perpendicular to the ice cliff surface:

$$\dot{b}_{icecliff} = \dot{b}_{backwasting} \cos(90 - \theta) \quad (8)$$

In the best case we assume a uniform ice cliff slope ($\theta$) for all ice cliffs of 48° based on the mean of slope measurements made at the top of each of the 60 ice cliffs where backwasting rates were measured in the study area (following Han et al., 2010). The mean of average ice cliff slopes from 6 other glaciers is 49° (Supplemental materials). Including the mean slope estimate from this study, the standard deviation of mean ice cliff slopes is 5°, which we use for our uncertainty estimates. In order to estimate the mass balance with elevation we integrate the contributions of ice cliff and sub-debris ablation across 50 meter elevation bands:

$$\bar{b}^i = \frac{\iint_{A^i_{debris}} \dot{b}_{debris}\, dx\, dy + \iint_{A^i_{icecliff}} \dot{b}_{icecliff}\, dx\, dy}{A^i} \quad (9)$$

where $\bar{b}^i$ is the mean ablation rate within the elevation band $i$ in units of m $d^{-1}$, $A^i_{debris}$ is the total debris-covered area, corrected for the surface slope of each debris-covered pixel using the 2013 WV-derived DEM discussed above, within the elevation band, $A^i_{icecliff}$ is the total ice cliff area, correcting for the slope of each ice cliff pixel based on the assumed ice cliff slope, within the elevation band, $A^i$ is the total planview area within the elevation band ,and $dx$ and $dy$ are both 0.5 m the original resolution of the WV imagery used for ice cliff delineation.

### 2.3.1 Uncertainty of distributed melt rates

We present one best distributed empirical melt estimate, which we bound with two extreme cases. These bounds are based on the compounding uncertainty of parameter choices meant to tilt the estimates in the direction of reduced or increased melt, this allows us to test the plausibility of ice cliffs leading to maximum melt within the zone of maximum thinning. For the best case the curve fits through debris thickness is calculated using the median of data from the 50-m elevation bins (Fig. 5). See Table 1 for the extreme parameters used for the distributed melt estimates. In the extreme cases for the debris thickness, curve fits were made through the 25% and 75% data points in each elevation bin. We use the interquartile range because the debris thickness within each elevation band is skewed towards values closer to 0, such that a normal distribution is not applicable (Fig. 5; Supplemental Material). We also apply $\pm 1\sigma$ range for sub-debris melt and ice cliff backwasting rates, and a $\pm 1\sigma$ range for ice cliffs slopes. Extreme ice cliff coverage was defined by ±20% of the bias corrected coverage within each elevation band. With these parameter choices 98.4 %% of all simulations lie inside the uncertainty range for combined sub-debris and ice cliff melt (Fig. 12).

In addition to the uncertainty evaluation presented here we also explore four additional cases in the supplemental materials. There we extrapolate debris thickness down each medial moraine using linear curve fits, using a single sigmoidal debris thickness-elevation relationship across the study area, using a linear relationship between backwasting and elevation, with even more uncertainties for each curve fit (in which the error envelope includes greater than 99.996 % of possibilities), and

with different debris thicknesses for the westernmost medial moraine. All explorations produce similar area-averaged melt-elevation relationships.

#### 2.3.2 Bare-ice melt rates extrapolated across the study area

For reference we also estimate the bare-ice melt rate through the study area for the summer of 2011, in the hypothetical case that no debris was present on the glacier. We calculate the bare-ice degree-day factor from several ablation stakes in bare-ice in the northeastern portion of the study area near 700 m a.s.l. We calculate the degree-day factor for ice (e.g., Hock, 2003) using measured bare-ice ablation and air temperatures interpolated onto the glacier (Supplementary material). We use hourly air temperature data from the Gates Glacier and May Creek meteorological stations to estimate the air temperature at each measurement location. Gates Glacier station is located just off the glacier margin at 1240 m a.s.l. and May Creek station is located at an 490 m a.s.l. located 15 km to the southwest of the town McCarthy (Fig. 1).

## 3 Results

### 3.1 In situ measurements

Figure 5 shows debris thickness as it varies with elevation. Debris thickness tends to increase downglacier and varies from less than a few millimeters above 700 m a.s.l. to as high as 1 meter above an ice cliff at 475 m a.s.l. (Table 2). Debris cover tends to be thicker in the medial moraines near the glacier margin, where ice margin retreat has been small (Fig. 4; Supplementary Figure 15). Debris greater than 40 cm thick was measured in medial moraine 3 above 600m a.s.l. And debris consistently 1 m thick was observed just out of the study area but still in moraine 9 at 730 m a.s.l. Toward the glacier interior and between 650 and 700 m a.s.l. debris thickness did not exceed 15 cm.

Debris thicknesses on glacier surfaces can vary by meters over 10-meter scales (e.g., Nicholson et al., 2018). Some of the scatter in our debris thickness measurements is derived from debris thickness variability caused by the local transport of debris by surface processes, in addition to the inevitable stochastic delivery from hillslopes above the glacier. 53 % of our debris thickness measurements were derived from the top of ice cliffs. This potentially biases our measurements toward thinner values because surface debris tends to be thicker in topographic lows.

Figure 6 shows the relationship between sub-debris melt rate and debris thickness (or Østrem's curve) during the study period (Table 2). Highly variable melt rates beneath debris less than 3 cm thick prevented the establishment of a relationship accounting for the melt-increasing effects of thin debris (e.g., Østrem, 1959).

The mean ice cliff backwasting rate was 7.1 cm $d^{-1}$ and the standard deviation for all measured ice cliffs was 2.5 cm $d^{-1}$. The maximum and minimum measured backwasting rate were 15 and 2.5 cm $d^{-1}$ respectively (Table 2). Figure 7 shows measured backwasting rates. While there is significant scatter within any elevation band a weak negative relationship between ice cliff backwasting and elevation is apparent (Supplemental Figure 7). Ice cliffs backwasted at rates similar rates with and without ponds and streams at their base and there is no apparent aspect dependence on backwasting rates (Fig. 7) .

### 3.2 Remotely-sensed ice cliff extent

#### 3.2.1 Performance of automatic ice cliff delineation methods

The adaptive binary threshold (*ABT*) method outperforms the Sobel edge delineation (*SED*) method. Averaged across the validation dataset, the *ABT* method correctly identifies 58% of ice cliff area, with 21% false positives. Percentages are relative to the hand-delineated validation dataset. The *SED* method yields a lower percentage of correctly identified ice cliffs (45%), but also produces fewer false positives (14%). In regions where we do not have manually digitized ice cliffs, our estimates of ice cliff area represent both true and false positives. Assuming our success rate is consistent across the glacier, we expect the *ABT* and *SED* approaches to detect 79% and 69% of the true ice cliff area, respectively.

Some systematic errors are evident, as anomalously light and dark regions of the glacier produce higher error. Regions of thin debris are especially problematic when using the *SED* method (Fig. 9; see also Herreid and Pellicciotti, 2018). To correct for this error in the *SED* results, where debris is very thin, we manually removed areas with highly erroneous ice cliff delineations; these only occur at higher elevations in the study area (Fig. 9). Due to its poorer performance, we do not use the *SED*-defined ice cliff area for the distributed mass balance estimates.

### 3.2.2 Spatial distribution of ice cliffs

The two delineation methods produce broadly similar ice cliff distributions. The *SED* method, specifically, overestimates ice cliff area at high elevation due to the thin, dark-colored debris. Over the 24.2 $km^2$ debris-covered portion of the study area, we estimate that ice cliffs cover 2.14 $km^2$ (8.8%) and 2.32 $km^2$ (9.7%) of ice cliff planview area using the *SED* and *ABT* methods, respectively (Fig. 10). If we apply a bias correction to the *SED* (31%) and *ABT* (21%) estimates based upon under-delineation rates in manually digitized areas, the ice cliffs cover 11.4% and 11.7% of the glacier respectively. Focusing on the *ABT* results, which provide the most accurate estimate, we find a "humped" profile in the elevational distribution of ice cliff fractional area. Ice cliff fractional area peaks between 520 and 620 m a.s.l. Below this elevation, ice cliff area decreases (Fig. 10).

In total, 11.7 % of the debris-covered tongue of Kennicott glacier is occupied by ice cliffs. See Anderson (2014) for an estimate using an independent method on Kennicott Glacier that is consistent. 11.7 % is 60% more coverage by percentage than on the Changri Nup Glacier, the glacier with the second highest coverage of ice cliffs studied to date (Table 4). The Kennicott Glacier has the lowest mean debris thickness (13 cm) of glaciers with reported ice cliff coverage percentages and supports, by far the highest percentage of ice cliffs. This implies that ice cliff coverage could vary with debris thickness or a variable that co-varies with debris thickness (Table 4).

We normalized ice cliff area by glacierized area within each elevation band, which we refer to as ice cliff fractional area. Ice cliff fractional area is relatively uniform at 7-8% except for a broad peak between 500-660 m a.s.l. within which fractional area reaches 13% at 540-560 m. The lower edge of this peak overlaps with the upper end of the *ZMT*.

### 3.3 Distributed estimates of melt

Figure 11 we show the best distributed estimate of melt split into sub-debris and ice cliff contributions across the study area. While sub-debris melt decreases toward the terminus due to thickening debris, we apply uniform ice cliff backwasting rates with the debris-covered portion of the study area.

When averaged across the entire study area, 8% of melt is derived from sub-debris melt and 26 (20 , 40 )% from ice cliff melt. Figure 12 shows that the insulating effects of debris cover is more important in setting the area-averaged melt rate than ice cliffs, especially where debris is typically thinner at higher elevations. Modeled bare ice melt rates, which are meant to represent the hypothetical melt rate if debris were absent from the study area, increase towards lower elevations and range from 5.9 to 7 cm $d^{-1}$ (Fig. 12). The dominance of decreasing sub-debris melt downglacier, due to thickening debris, results in a deviation from the bare-ice melt rate above 700 m a.s.l. (relative to the 2013 glacier surface). Elevation-band averaged sub-debris melt rates decline from 4.2 cm $d^{-1}$ (3.2, 5.1) at the top of the study area to 1.6 cm $d^{-1}$ (0.98, 2.0) near the terminus.

Ice cliffs, when their total melt contribution is averaged over entire elevation bands, produced rates of 0.73 cm $d^{-1}$ (0.31, 1.29) at the top of the study area and 0.69 cm $d^{-1}$ (0.33, 1.4) near the terminus. The maximum contribution of ice cliffs to band-averaged melt occurs near 500 m and has a value of 1.3 cm $d^{-1}$ (0.58, 2.4). Ice cliffs contribute most to mass loss in the 500 to 520 m a.s.l. elevation band, close to where the ice cliff fractional area also maximizes. Ice cliffs between 500 and 520 m a.s.l. generate the highest percentage 42% (34, 58%) of the total mass loss due to ice cliffs and sub-debris melt within the study area.

## 4 Discussion

### 4.1 Field measurements

Our ablation stake derived sub-debris melt rates are highly variable beneath debris less than 3 cm (Fig. 5). It appears that local environmental conditions are as important as the potential for melt enhancement due to thin debris (see Mihalcea et al., 2006; Reid and Brock, 2010 for similar observations). Our measured sub-debris melt rates are consistent with the observations made by Fyffe et al. (2020): a consistent melt enhancing effect due to debris less than 3 cm is not apparent. Debris typically forms parabolic-shaped medial moraines in cross-section (e.g., Anderson, 2000) suggesting that the melt suppressing effect of debris dominates, in the study area (and upglacier as well). Despite this the melt enhancing effect of debris less than 3 cm remains an important potential melt-enhancing effect of debris cover, that is most likely to increase surface melt at the upglacier end of debris covers.

Based on our debris thickness to sub-debris melt measurements, the characteristic debris thickness ($h_*$) was 8.17 cm. Practically an $h_*$ of 8.17 cm means that sub-debris melt rate will be 50% of the bare ice melt rate at 8.17 cm debris thickness (Eqn. 4). The relationship between melt rate and debris thickness from Kennicott Glacier is similar to those derived from

other debris-covered glaciers at similar latitudes (Supplemental Material). The consistent decline in sub-debris melt rates as debris thickens is not unexpected considering that the global mean value of $h_*$ is 6.6 ± 2.9 m (1 σ )(based on 15 glaciers from Anderson and Anderson, 2014).

Significant scatter is present in the ice cliff backwasting rates as they vary with elevation, suggesting that controls independent of elevation are important. But when our backwasting rate data are binned in 50 m elevation bands a weak increase in backwasting rates towards lower elevations is apparent. Potential causes of higher backwasting rates at lower elevations are: 1) increased air temperatures. Increased debris thickness leads to higher debris surface temperatures, longwave fluxes, and energy available for melt (e.g., Brock et al., 2010); or 2) increased debris veneers and lower ice cliff albedo at low elevations (e.g., Reid and Brock, 2014). Because ice cliffs, by definition persist above the angle of repose, large clasts (pebble-sized and larger) tend to trundle to the base of ice cliffs. But fine materials (clay and sand sized particles) on the other hand are more likely to persist on steep ice cliff surfaces. This could be due to local surface roughness on the ice cliff allowing for fine material to accumulate. For finer grains attractive inter particle surface forces, frictional interlocking of grain aggregates, and electrochemical forces are more likely to adhere debris to cliff surfaces (e.g., Jain and Kothyari, 2009; Supplementary Photos 1-3). When melt is occurring on the ice cliff, the adhesive and cohesive properties of liquid water may also also help retain fine debris on cliff surfaces. It follows that fine debris will be more likely to decrease ice cliff albedo where debris cover above ice cliffs are composed of more fine material. It has been noted in several studies of debris cover grain size that the percentage of fine material composing debris covers tends to increase towards glacier termini (Owen et al., 2003; Kellerer-Pirklbauer, 2008).

Thicker debris cover leads to higher debris surface temperatures, and higher longwave radiation fluxes received by ice cliffs. Despite this physical relationship, the backwasting rates measured on Kennicott Glacier are similar to those measured on glaciers with thicker debris cover and at lower latitude (Table 3). The similarity in backwasting rates suggests that there may be compensating effects between latitude, day length, and altitude. i.e., Himalayan glaciers are present at a lower latitude but they also tend to persist at high elevations compared to, for example, Kennicott Glacier which persists at a much higher latitude but also lower elevation. Ultimately the lack of aspect control on backwasting rates on Kennicott Glacier contrasts with observations from lower latitudes (e.g., Buri and Pellicciotti, 2018), suggesting that there may be a latitudinal control on ice cliff backwasting rates as they vary with orientation.

In this study, backwasting was measured at the top of ice cliffs. Based on the modeling of Buri et al. (2016b) from Lirung Glacier, Nepal (28° N), the highest backwasting rates tend to occur near the top of ice cliffs (noting that only northwest and northeast facing ice cliffs were modeled). But making in situ measurements across a representative population of ice cliffs is very difficult. We assume that a single measurement from 60 ice cliffs would better represent the mean backwasting rate across the thousands of ice cliffs in the study area. The validity of this assumption should be explored in future field campaigns. If it is true that ice cliff backwasting is maximized at the top of ice cliffs then distributed estimates of surface melt using our backwasting rates could overestimate ice cliff backwasting when averaged across entire cliffs. It could be that our ice cliff backwasting rates overestimate the melt potentially skewing our estimates towards higher than actual melt rates in the zone of maximum thinning.

### 4.2 Ice cliff delineation methods

Our automated methods provide an accurate estimate of ice cliff area, though both the *ABT* and *SED* ice cliff delineation methods underpredict ice cliff area, without bias corrections. These methods require that ice cliffs are dark relative to surrounding debris cover. This observation of darker ice cliffs is generally true for Kennicott and several other debris covered glaciers we examined, but this relationship should be verified before application different glaciers. Output should simply be examined to ensure that such conditions do not contaminate results. Ice cliffs may be brighter than the surrounding debris if the ice cliffs are not covered with thin debris films or if they are strongly illuminated. Our method will therefore likely underpredict south-facing ice cliffs, although we observe many correct delineations.

Future improvements to these delineation methods may be achieved using more advanced image segmentation techniques (e.g., Leyk and Boesch, 2010), by utilizing image texture analysis, or by adaptively changing image processing parameters within a window moving across the image and mosaicing the results. The transferability of optimal processing parameters (both across time and space) requires further investigation, but none-the-less we present a promising approach for the large-scale delineation of ice cliffs. Using multispectral imagery would also likely improve delineation, although such imagery is less readily available. The delineation methods presented here could be compared to the cliff delineation algorithm of Herreid and Pellicciotti (2018) using existing high-resolution DEMs on Kennicott Glacier.

### 4.3 Distributed estimates of melt

On Kennicott Glacier, ice cliffs most likely contribute 26% (with extreme bounds of 20 and 40%) of melt of the debris-covered tongue. This percentage is more than twice the percentages reported from other glaciers with mean debris thicknesses less than 50 cm (Table 4). This is likely due to the high fractional coverage of ice cliffs on the Kennicott Glacier. For glaciers with mean debris thicknesses much larger than 50 cm, ice cliff contributions are larger than 26% and are as high as 40%. For these other glaciers high ice cliff contributions occur despite much lower ice cliff coverage compared to Kennicott Glacier (Table 4). It follows that relative ice cliff contribution will be higher where sub-debris melt rates are low.

Ice cliffs tend to contribute a higher fraction of mass loss as debris thickness increases. This trend is visible on Kennicott Glacier as debris thickens toward the terminus (Fig. 12). This relationship also appears to hold when considering debris-covered glaciers from different regions (Table 4). As debris thickens the contribution of ice cliff melt also tends to increase. This appears to occur even though the fractional coverage of ice cliffs tends to decrease as mean debris thicknesses increase.

Ice cliffs do not counteract the insulating effects of debris on Kennicott Glacier (Fig. 12). The thin debris within the study area leads to melt rates closer to bare-ice melt rates than most other studied debris-covered glaciers. Measured ice cliff backwasting rates are comparable or higher than measurements from other studies (Table 3. Kennicott Glacier also has the highest fractional coverage of ice cliffs, relative to other studied glaciers, which also serves to increase melt rates (Table 4). Despite this, ice cliffs on Kennicott Glacier do not compensate for the insulating effects of debris. This suggests that the presence of ice cliffs is unlikely to counter the insulating effects of debris on glaciers with thicker debris and/or lower ice cliff coverage.

#### 4.3.1 *Do ice cliffs maximize melt in the ZMT in the summer of 2011?*

During the measurement period between mid June and mid August of 2011, the melt within the zone of maximum thinning (*ZMT*) is strongly suppressed by insulating debris cover. For this discussion we make the assumption that the *ZMT* – which was stable between the 1957 to 2004 and 2000 to 2007 time periods-- remained in the same location during summer of 2011. Note that from 1957 to present the *ZMT* of Kennicott Glacier has been debris covered (Supplemental Figure 26). All explored debris thickness extrapolation approaches presented here show that the melt profile is strongly suppressed by thick debris, a pattern that remains consistent even when extreme parameters are chosen to increase the melt rate of ice cliffs (Supplemental Material). All of these estimates also include the potential slight biases of our measurements towards 1) thinner debris, and 2) high backwasting rates. We further assess what changes in debris thickness, sub-debris melt rate, ice cliff coverage, or backwasting rates would be required to produce the highest glacier-wide melt rates within the *ZMT*. The point of this exercise is to show how extreme the parameter choices would be to maximize melt within the *ZMT*.

*Debris cover and sub-debris melt:* Debris thickness would have to decrease, specifically in the *ZMT,* from ~20 cm to 2 cm (a reduction factor of 0.1) to produce maximum glacier-wide melt rates there. 53 % of our debris thickness measurements were derived from the top of ice cliffs and topographic highs. Because debris tends to concentrate in topographic lows our debris thickness measurements may be biased toward thinner debris, making the required reduction in debris thickness even more extreme. Melt would also be maximized in the zone of maximum thinning, where measured debris is ~20 cm thick, sub-debris melt rates would have to increase from ~ 1.6 cm $d^{-1}$ by a factor of 3 to 4.8 cm $d^{-1}$.

*Ice Cliffs*: In order for ice cliffs, in the *ZMT*, to enhance melt and produce maximum glacier-wide melt rates in the *ZMT*, backwasting rates would need to be 6.5 times higher than those measured in the summer of 2011. Our backwasting estimates are based on repeated measurements at a single location at the top of each ice cliff. Maximum backwasting rates across each ice cliff are more likely to occur near the top (Buri et al., 2016). Applying our measurements across single ice cliffs or the entire ice cliff population may therefore overestimate ice cliff melt. The hypothetical backwasting rates required to maximize melt in the *ZMT* are therefore unreasonable; a compilation of previously published backwasting rates in Table 3 support this.

In order for ice cliffs in the *ZMT* to compensate for the insulating effects of debris and enhance melt in the *ZMT* beyond bare ice melt rates, ice cliff area would need to increase from 11.7% to 90% of the glacier surface. This again suggests that ice cliff melt does not control the location of the *ZMT* at least during the summer of 2011.

### 4.4 Østrem's curve expressed in the mass balance profile

On debris-covered glacier termini, debris tends to thicken towards debris-covered glacier termini (e.g., Anderson and Anderson, 2018) as is the case for Kennicott Glacier**.** This leads to the expectation that sub-debris melt rates will decline towards the terminus reversing the mass balance gradient, similar to the results and conclusions for glaciers in the Khumbu

of Nepal (Bisset et al., 2020). The overall mass balance profile for the summer of 2011 (Fig. 12) shows this Østrem's curve like pattern, suggesting that it is more strongly influenced by debris thickness than melt hotspots. Future efforts to represent the effects of ice cliffs on glacier mass balance at the regional scale could consider using a modified debris thickness-melt relationship with a percentage enhancement based on empirical relationships between debris thickness and ice cliff melt contribution. Even where ice cliffs contribute 42 % of melt the surface mass balance pattern still largely follows Østrem's curve.

**5 Conclusions**

The melt within a debris-covered tongue of a large Alaskan Glacier has been quantified. We conclude that:

- For Kennicott Glacier the zone of glacier-wide maximum thinning occurs under melt-reducing debris cover, up-glacier from its terminus. Based on the periods 1957-2004 and 2000-2007 the zone of maximum thinning appears to be in a stable location (Das et al., 2014) and has been continuously debris covered since at least 1957.
- Kennicott Glacier is covered by thinner debris than most previously studied glaciers (mean debris thickness of ~14 cm). Debris thickness tends to increase down glacier. It is thickest near the terminus near the margin of Kennicott Glacier.
- We see significant scatter in melt rates for debris under 3 cm thick. In some locations melt is amplified relative to bare ice melt rates and in others melt is suppressed, suggesting that local glacier surface hydrology or meteorology may be important in determining whether or not melt amplification occurs under debris less than 3 cm thick.
- Measured ice cliff backwasting rates from Kennicott Glacier are as high as those measured from any other glacier measured to date. We find no consistent control of backwasting rate by orientation, or whether streams or ponds are present at the base of the ice cliff. More measurements are needed to robustly test these results. A slight dependence of backwasting rate with elevation may be present, although there is considerable variability within any elevation band.
- A new ice cliff delineation method is presented using high-resolution panchromatic WorldView1 satellite imagery. This method provides a robust estimate of ice cliff extent for a particularly difficult test case in which ice cliffs are abundant, and often small. The method is robust even as debris surface color varies across 9 medial moraines.
- Within its debris-covered tongue, Kennicott Glacier hosts the highest percentage of ice cliffs by area (11.7%) of any previously studied glacier.
- Abundant in situ measurements allow extrapolation of debris thickness, sub-debris melt, and ice cliff backwasting, across the study area. Debris thicknesses are extrapolated down individual flow paths.
- During the summer of 2011, approximately 26% of melt in the entire debris-covered tongue is attributable to ice cliffs while covering 11.7% of the study area. In the lowest 4 kilometers of Kennicott Glacier where debris tends to be thicker than 15 cm and hence sub-debris melt rates are low, ice cliffs constitute up to 42% of melt.
- Ice cliffs strongly contribute to the surface melt of Kennicott glacier. Ice cliffs contribute a larger percentage of mass loss in places where debris cover is thick, a pattern observed across the Kennicott Glacier and for other studied glaciers from other regions.
- The mass balance profile within the debris covered portion of the glacier appears to follow the debris-melt relationship or Østrem's curve.
- If surface melt was the sole control on the location of the zone of maximum thinning (*ZMT*) then surface melt must peak within the *ZMT*. The thin debris, high ice cliff backwasting rates, and abundant of ice cliffs found on the debris-covered tongue of Kennicott Glacier (relative to previously studied debris-covered glaciers) all suggest that the ice cliffs should compensate for the melt-suppressing effects of debris (relative to bare-ice melt rates). However even with extreme parameter choices and extreme uncertainty scenarios melt rates in the zone of maximum thinning, neither match hypothetical bare-ice melt rates at the same elevation nor result in glacier-wide maximum melt rates within the *ZMT*.
- Because melt hotspots do not appear to control the *ZMT* location, during the study period, we suggest that ice dynamics and the decline in ice discharge from upglacier appears to be vital to explain high glacier thinning rates despite thick, melt-insulating debris cover.

**Data availability**

Datasets and results are available upon request.

**Author contribution statement**

LSA, WHA, and RSA designed the study. LSA composed the manuscript, collected all field data, and completed all analyses besides the automatic ice cliff delineation method. WHA developed the ice cliff delineation method, delineated ice cliffs, and wrote the associated text. RSA advised LSA and WHA through the study and contributed to the text and figures. PB contributed to the text and added important discussion that improved the manuscript. All authors aided in composing the manuscript.

**Competing Interests**

The authors declare that they have no conflict of interest.

**Acknowledgements**

We thank Francesca Pellicciotti for her considerable efforts in editing this manuscript as well as Evan Miles, David Rounce, and two anonymous reviewers whose comments significantly improved the full body of work. LSA acknowledges support from a 2011 Muire Science and Learning Center Fellowship, NSF DGE-1144083 (GRFP), and funding from the European Research Council (ERC) under the European Union's Horizon 2020 research and innovation programme under grant agreement No 759639. RSA and WHA acknowledge support of NSF EAR-1239281 (Boulder Creek CZO) and NSF EAR-1123855. WHA acknowledges support from NSF OPP-1821002 and the University of Colorado at Boulder's Earth Lab initiative. We thank Craig Anderson, Emily Longano, and Oren Leibson for invaluable field support. We thank Indrani Das, Regine Hock, Martin Truffer, Jack Holt, Eric Peterson, Brandon Tober, Dirk Scherler, Katy Barnhart, Andy Wickert, and Eric Winchell for thoughtful discussions. LSA thanks the organizers and participants of the 2010 Glaciological Summer School held in McCarthy, Alaska, which inspired this research. We thank Per Jenssen, Susan Fison, Ben Hudson, Patrick Tomco, Rommel Zulueta, the Wrangell-St. Elias Interpretive Rangers, the Wrangell Mountains Center, and Ted Scambos (NSIDC) for logistical support and the gracious loan of equipment. We thank Lucy Tyrell for facilitating outreach efforts. We also thank Joshua Scott, Wrangell-St Elias National Park and the Polar Geospatial Center for access to satellite imagery as well as Etienne Berthier for sharing DEMs. WHA thanks Waleed Abdalati, Mahsa Mousavi, and Stefan Leyk for guidance in image processing.

**References**

Agarwal, V., Bolch, T., Syed, T. H., Pieczonka, T., Strozzi, T. and Nagaich, R.: Area and mass changes of Siachen Glacier (East Karakoram), Journal of Glaciology, 63(237), 148–163, doi:10.1017/jog.2016.127, 2017.

Anderson, L. S.: Glacier Response to Climate Change: Modeling the Effects of Weather and Debris-Cover, Dissertation, Geological Sciences, University of Colorado, Boulder, December. [online] Available from: https://scholar.colorado.edu/geol_gradetds/90, 2014.

Anderson, L. S. and Anderson, R. S.: Modeling debris-covered glaciers: response to steady debris deposition, The Cryosphere, 10(3), 1105–1124, doi:10.5194/tc-10-1105-2016, 2016.

Anderson, L. S. and Anderson, R. S.: Debris thickness patterns on debris-covered glaciers, Geomorphology, 311, 1–12, doi:10.1016/j.geomorph.2018.03.014, 2018.

Armstrong, W. H., Anderson, R. S. and Fahnestock, M. A.: Spatial Patterns of Summer Speedup on South Central Alaska Glaciers: Patterns of Glacier Summer Speedup, Geophysical Research Letters, 44(18), 9379–9388, doi:10.1002/2017GL074370, 2017.

Benn, D. I., Bolch, T., Hands, K., Gulley, J., Luckman, A., Nicholson, L. I., Quincey, D., Thompson, S., Toumi, R. and Wiseman, S.: Response of debris-covered glaciers in the Mount Everest region to recent warming, and implications for outburst flood hazards, Earth-Science Reviews, 114(1–2), 156–174, doi:10.1016/j.earscirev.2012.03.008, 2012.

Berthier, E., Schiefer, E., Clarke, G. K. C., Menounos, B. and Rémy, F.: Contribution of Alaskan glaciers to sea-level rise derived from satellite imagery, Nature Geoscience, 3(2), 92–95, doi:10.1038/ngeo737, 2010.

Bisset, R. R., Dehecq, A., Goldberg, D. N., Huss, M., Bingham, R. G. and Gourmelen, N.: Reversed Surface-Mass-Balance Gradients on Himalayan Debris-Covered Glaciers Inferred from Remote Sensing, Remote Sensing, 12(10), 1563, doi:10.3390/rs12101563, 2020.

Brock, B. W., Mihalcea, C., Kirkbride, M. P., Diolaiuti, G., Cutler, M. E. J. and Smiraglia, C.: Meteorology and surface energy fluxes in the 2005–2007 ablation seasons at the Miage debris-covered glacier, Mont Blanc Massif, Italian Alps, Journal of Geophysical Research, 115(D9), doi:10.1029/2009JD013224, 2010.

Brun, F., Buri, P., Miles, E. S., Wagnon, P., Steiner, J., Berthier, E., Ragettli, S., Kraaijenbrink, P., Immerzeel, W. W. and Pellicciotti, F.: Quantifying volume loss from ice cliffs on debris-covered glaciers using high-resolution terrestrial and aerial photogrammetry, Journal of Glaciology, 62(234), 684–695, doi:10.1017/jog.2016.54, 2016.

Brun, F., Wagnon, P., Berthier, E., Shea, J. M., Immerzeel, W. W., Kraaijenbrink, P. D. A., Vincent, C., Reverchon, C., Shrestha, D. and Arnaud, Y.: Ice cliff contribution to the tongue-wide ablation of Changri Nup Glacier, Nepal, central Himalaya, The Cryosphere, 12(11), 3439–3457, doi:10.5194/tc-12-3439-2018, 2018.

Buri, P. and Pellicciotti, F.: Aspect controls the survival of ice cliffs on debris-covered glaciers, Proceedings of the National Academy of Sciences, 115(17), 4369–4374, doi:10.1073/pnas.1713892115, 2018.

Buri, P., Pellicciotti, F., Steiner, J. F., Miles, E. S. and Immerzeel, W. W.: A grid-based model of backwasting of supraglacial ice cliffs on debris-covered glaciers, Annals of Glaciology, 57(71), 199–211, doi:10.3189/2016AoG71A059, 2016.

Das, I., Hock, R., Berthier, E. and Lingle, C. S.: 21st-century increase in glacier mass loss in the Wrangell Mountains, Alaska, USA, from airborne laser altimetry and satellite stereo imagery, Journal of Glaciology, 60(220), 283–293, doi:10.3189/2014JoG13J119, 2014.

Dougherty, E. R.: An Introduction to Morphological Image Processing (Tutorial Texts in Optical Engineering, DC O'Shea, SPIE Optical Engineering Press, Bellingham, WA, USA, 1992.

Gardelle, J., Berthier, E., Arnaud, Y. and Kääb, A.: Corrigendum to "Region-wide glacier mass balances over the Pamir-Karakoram-Himalaya during 1999–2011" published in The Cryosphere, 7, 1263–1286, 2013, The Cryosphere, 7(6), 1885–1886, doi:10.5194/tc-7-1885-2013, 2013.

Han, H., Wang, J., Wei, J. and Liu, S.: Backwasting rate on debris-covered Koxkar glacier, Tuomuer mountain, China, Journal of Glaciology, 56(196), 287–296, doi:10.3189/002214310791968430, 2010.

Herreid, S. and Pellicciotti, F.: Automated detection of ice cliffs within supraglacial debris cover, The Cryosphere, 12(5), 1811–1829, doi:10.5194/tc-12-1811-2018, 2018.

Hock, R.: Temperature index melt modelling in mountain areas, Journal of Hydrology, 282(1–4), 104–115, doi:10.1016/S0022-1694(03)00257-9, 2003.

Immerzeel, W. W., Kraaijenbrink, P. D. A., Shea, J. M., Shrestha, A. B., Pellicciotti, F., Bierkens, M. F. P. and de Jong, S. M.: High-resolution monitoring of Himalayan glacier dynamics using unmanned aerial vehicles, Remote Sensing of Environment, 150, 93–103, doi:10.1016/j.rse.2014.04.025, 2014.

Jain, R. K. and Kothyari, U. C.: Cohesion influences on erosion and bed load transport: INFLUENCE OF COHESION, Water Resources Research, 45(6), doi:10.1029/2008WR007044, 2009.

Juen, M., Mayer, C., Lambrecht, A., Han, H. and Liu, S.: Impact of varying debris cover thickness on ablation: a case study for Koxkar Glacier in the Tien Shan, The Cryosphere, 8(2), 377–386, doi:10.5194/tc-8-377-2014, 2014.

Kääb, A., Berthier, E., Nuth, C., Gardelle, J. and Arnaud, Y.: Contrasting patterns of early twenty-first-century glacier mass change in the Himalayas, Nature, 488(7412), 495–498, doi:10.1038/nature11324, 2012.

Kellerer-Pirklbauer, A.: The Supraglacial Debris System at the Pasterze Glacier, Austria: Spatial Distribution, Characteristics and Transport of Debris, Zeitschrift für Geomorphologie, Supplementary Issues, 52(1), 3–25, doi:10.1127/0372-8854/2008/0052S1-0003, 2008.

Kirkbride, M. P.: The temporal significance of transitions from melting to calving termini at glaciers in the central Southern Alps of New Zealand, The Holocene, 3(3), 232–240, doi:10.1177/095968369300300305, 1993.

Kraaijenbrink, P. D. A., Shea, J. M., Pellicciotti, F., Jong, S. M. de and Immerzeel, W. W.: Object-based analysis of unmanned aerial vehicle imagery to map and characterise surface features on a debris-covered glacier, Remote Sensing of Environment, 186, 581–595, doi:10.1016/j.rse.2016.09.013, 2016.

Lamsal, D., Fujita, K. and Sakai, A.: Surface lowering of the debris-covered area of Kanchenjunga Glacier in the eastern Nepal Himalaya since 1975, as revealed by Hexagon KH-9 and ALOS satellite observations, The Cryosphere, 11(6), 2815–2827, doi:10.5194/tc-11-2815-2017, 2017.

Larsen, C. F., Burgess, E., Arendt, A. A., O'Neel, S., Johnson, A. J. and Kienholz, C.: Surface melt dominates Alaska glacier mass balance: Alaska Glacier Mass Balance, Geophysical Research Letters, 42(14), 5902–5908, doi:10.1002/2015GL064349, 2015.

Leyk, S. and Boesch, R.: Colors of the past: color image segmentation in historical topographic maps based on homogeneity, GeoInformatica, 14(1), 1, 2010.

Mihalcea, C., Mayer, C., Diolaiuti, G., Lambrecht, A., Smiraglia, C. and Tartari, G.: Ice ablation and meteorological conditions on the debris-covered area of Baltoro glacier, Karakoram, Pakistan, Annals of Glaciology, 43, 292–300, doi:10.3189/172756406781812104, 2006.

Miles, E. S., Pellicciotti, F., Willis, I. C., Steiner, J. F., Buri, P. and Arnold, N. S.: Refined energy-balance modelling of a supraglacial pond, Langtang Khola, Nepal, Annals of Glaciology, 57(71), 29–40, doi:10.3189/2016AoG71A421, 2016.

Miles, E. S., Willis, I., Buri, P., Steiner, J. F., Arnold, N. S. and Pellicciotti, F.: Surface Pond Energy Absorption Across Four Himalayan Glaciers Accounts for 1/8 of Total Catchment Ice Loss, Geophysical Research Letters, 45(19), 10,464-10,473, doi:10.1029/2018GL079678, 2018.

Mölg, N., Bolch, T., Walter, A. and Vieli, A.: Unravelling the evolution of Zmuttgletscher and its debris cover since the end of the Little Ice Age, The Cryosphere, 13(7), 1889–1909, doi:10.5194/tc-13-1889-2019, 2019.

Nuimura, T., Fujita, K., Yamaguchi, S. and Sharma, R. R.: Elevation changes of glaciers revealed by multitemporal digital elevation models calibrated by GPS survey in the Khumbu region, Nepal Himalaya, 1992-2008, Journal of Glaciology, 58(210), 648–656, doi:10.3189/2012JoG11J061, 2012.

Nye, J. F.: The response of glaciers and ice-sheets to seasonal and climatic changes, Proceedings of the Royal Society of London. Series A. Mathematical and Physical Sciences, 256(1287), 559–584, doi:10.1098/rspa.1960.0127, 1960.

Østrem, G.: Ice melting under a thin layer of moraine, and the existence of ice cores in moraine ridges, Geografiska Annaler, 41(4), 228–230, 1959.

Owen, L. A., Derbyshire, E. and Scott, C. H.: Contemporary sediment production and transfer in high-altitude glaciers, Sedimentary Geology, 155(1–2), 13–36, doi:10.1016/S0037-0738(02)00156-2, 2003.

Pellicciotti, F., Stephan, C., Miles, E., Herreid, S., Immerzeel, W. W. and Bolch, T.: Mass-balance changes of the debris-covered glaciers in the Langtang Himal, Nepal, from 1974 to 1999, Journal of Glaciology, 61(226), 373–386, doi:10.3189/2015JoG13J237, 2015.

Pfeffer, W. T., Arendt, A. A., Bliss, A., Bolch, T., Cogley, J. G., Gardner, A. S., Hagen, J.-O., Hock, R., Kaser, G., Kienholz, C., Miles, E. S., Moholdt, G., Mölg, N., Paul, F., Radić, V., Rastner, P., Raup, B. H., Rich, J., Sharp, M. J. and The Randolph Consortium: The Randolph Glacier Inventory: a globally complete inventory of glaciers, Journal of Glaciology, 60(221), 537–552, doi:10.3189/2014JoG13J176, 2014.

Racoviteanu, A. and Williams, M. W.: Decision Tree and Texture Analysis for Mapping Debris-Covered Glaciers in the Kangchenjunga Area, Eastern Himalaya, Remote Sensing, 4(10), 3078–3109, doi:10.3390/rs4103078, 2012.

Reed, P. M., Hadka, D., Herman, J. D., Kasprzyk, J. R. and Kollat, J. B.: Evolutionary multiobjective optimization in water resources: The past, present, and future, Advances in water resources, 51, 438–456, 2013.

Reid, T. D. and Brock, B. W.: An energy-balance model for debris-covered glaciers including heat conduction through the debris layer, Journal of Glaciology, 56(199), 903–916, doi:10.3189/002214310794457218, 2010.

Reid, T. D. and Brock, B. W.: Assessing ice-cliff backwasting and its contribution to total ablation of debris-covered Miage glacier, Mont Blanc massif, Italy, Journal of Glaciology, 60(219), 3–13, doi:10.3189/2014JoG13J045, 2014.

Richards, J. A.: Remote Sensing Digital Image Analysis, Fifth., Springer-Verlag, Berlin., 2013.

Rickman, R. L. and Rosenkrans, D. S.: Hydrologic Conditions and Hazards in the Kennicott River Basin, Wrangell-St. Elias National Park and Preserve, Alaska, Water-Resources Investigations Report, U.S. Geological Survey, Anchorage, Alaska., 1997.

Sakai, A., Nakawo, M. and Fujita, K.: Melt rate of ice cliffs on Lirung Glacier, Nepal Himalayas, 1996, Bulletin of Glacier Research, 16, 57–66, 1998.

Sakai, A., Nakawo, M. and Fujita, K.: Distribution Characteristics and Energy Balance of Ice Cliffs on Debris-covered Glaciers, Nepal Himalaya, Arctic, Antarctic, and Alpine Research, 34(1), 12–19, doi:10.1080/15230430.2002.12003463, 2002.

Sauvola, J. and Pietikäinen, M.: Adaptive document image binarization, Pattern Recognition, 33(2), 225–236, doi:10.1016/S0031-3203(99)00055-2, 2000.

Scherler, D., Wulf, H. and Gorelick, N.: Global Assessment of Supraglacial Debris-Cover Extents, Geophysical Research Letters, 45(21), 11,798-11,805, doi:10.1029/2018GL080158, 2018.

Shean, D. E., Alexandrov, O., Moratto, Z. M., Smith, B. E., Joughin, I. R., Porter, C. and Morin, P.: An automated, open-source pipeline for mass production of digital elevation models (DEMs) from very-high-resolution commercial stereo satellite imagery, ISPRS Journal of Photogrammetry and Remote Sensing, 116, 101–117, 2016.

Steiner, J. F., Pellicciotti, F., Buri, P., Miles, E. S., Immerzeel, W. W. and Reid, T. D.: Modelling ice-cliff backwasting on a debris-covered glacier in the Nepalese Himalaya, Journal of Glaciology, 61(229), 889–907, doi:10.3189/2015JoG14J194, 2015.

Thompson, S., Benn, D. I., Mertes, J. and Luckman, A.: Stagnation and mass loss on a Himalayan debris-covered glacier: processes, patterns and rates, Journal of Glaciology, 62(233), 467–485, doi:10.1017/jog.2016.37, 2016.

Tielidze, L. G., Bolch, T., Wheate, R. D., Kutuzov, S. S., Lavrentiev, I. I. and Zemp, M.: Supra-glacial debris cover changes in the Greater Caucasus from 1986 to 2014, The Cryosphere, 14(2), 585–598, doi:10.5194/tc-14-585-2020, 2020.

Vincent, C., Wagnon, P., Shea, J., Immerzeel, W., Kraaijenbrink, P., Shrestha, D., Soruco, A., Arnaud, Y., Brun, F., Berthier, E. and Sherpa, S.: Reduced melt on debris-covered glaciers: investigations from Changri Nup Glacier, Nepal, The Cryosphere, 15, 2016.

Watson, C. S., Quincey, D. J., Carrivick, J. L. and Smith, M. W.: Ice cliff dynamics in the Everest region of the Central Himalaya, Geomorphology, 278, 238–251, doi:10.1016/j.geomorph.2016.11.017, 2017.

Wu, K., Liu, S., Jiang, Z., Xu, J., Wei, J. and Guo, W.: Recent glacier mass balance and area changes in the Kangri Karpo Mountains from DEMs and glacier inventories, The Cryosphere, 12(1), 103–121, doi:10.5194/tc-12-103-2018, 2018.

Yapo, P. O., Gupta, H. V. and Sorooshian, S.: Multi-objective global optimization for hydrologic models, Journal of hydrology, 204(1–4), 83–97, 1998.

Zhang, Y., Fujita, K., Liu, S., Liu, Q. and Nuimura, T.: Distribution of debris thickness and its effect on ice melt at Hailuogou glacier, southeastern Tibetan Plateau, using in situ surveys and ASTER imagery, Journal of Glaciology, 57(206), 1147–1157, doi:10.3189/002214311798843331, 2011.

600

**Tables**

**Table 1.** Parameters used for the best distributed melt and uncertainty estimates

| Parameter name | Parameter symbol | Min. | Best | Max. | |
|---|---|---|---|---|---|
| Debris thickness [cm] | a | 17.6 | 21.55 | 34.3 | Interquartile range |
| | b | 0.016 | 0.13 | 0.01 | |
| | c | 538 | 551 | 556 | |
| | d | 2.1 | 2.1 | 2.6 | |
| Sub-debris melt rate [cm $d^{-1}$] | $\dot{b}_{ice}$ | 4.87 | 5.87 | 6.87 | ± 1σ |
| | $h_*$ | 8.17 | 8.17 | 8.17 | |
| Ice cliff backwasting [cm $d^{-1}$] | f | 2.18 | 7.1 | 12.0 | ± 1 σ |
| Ice cliff slope [degree] | θ | 43 | 48 | 53 | ± 1σ |

**Table 2.** Statistics of debris- and melt-related measurements for Kennicott Glacier

| Measured variable | Mean | Std. | Minimum | Maximum |
|---|---|---|---|---|
| Debris thickness [cm] | 13.7 | 13.9 | 0 | 100 |
| Sub-debris ablation [cm $d^{-1}$] | 4.0 | 1.8 | 0.8 (37 cm of debris) | 7.3 (1 cm of debris) |
| Ice cliff backwasting [cm $d^{-1}$] | 7.1 | 2.5 | 2.8 | 13.8 |

605

**Table 3.** Comparison of ice cliff backwasting rates and debris thicknesses with other glaciers

| Glacier | Region | Latitude [deg.] | Mean study area elevation [m] | Range of backwasting rates [cm $d^{-1}$] | Mean debris thickness [cm] | Reference |
|---|---|---|---|---|---|---|
| Kennicott | Alaska | 61 | 600 | 3-15 | 13 | This study |
| Miage | Alps, Italy | 46 | 2200 | 6.1-7.5 | 26 | Reid and Brock, 2014 |
| Koxkar | Tien Shan, China | 42 | 3500 | 3-10 | 53 | Han et al., 2010; Juen et al., 2014 |
| Lirung | Himalaya, Nepal | 28 | 4200 | 7-11 | 50-100 | Brun et al., 2016 |
| Changri Nup | Himalaya, Nepal | 28 | 5400 | 2.2-4.5 | - | Brun et al., 2018 |

*Sorted by latitude

**Table 4.** Comparison of ice cliff coverage and melt contribution with other debris-covered glaciers

| Glacier | Region | Ice cliff fractional area (%)** | Ice cliff mass loss (%) | Mean debris thickness [cm] | Study |
|---|---|---|---|---|---|
| Ngozumpa | Himalaya, Nepal | 5 | 40 | 0-300 | Thompson et al., 2016 |
| Lirung | Himalaya, Nepal | 2.0 | 36 | 50-100 | Buri and Pellicciotti, 2018 |
| Changri Nup | Himalaya, Nepal | 7.4 | 24 (±5) | - | Brun et al., 2018 |
| Langtang | Himalaya, Nepal | 1.3 | 20 | - | Buri and Pellicciotti, 2018 |
| Kennicott | Alaska | 11.7 | 20 (±8) | 13 | This study |
| Koxkar | Tien Shan, China | 1.4 | 7.4-12 | 53 | Han et al., 2010; Juen et al., 2014 |
| Miage | Alps, Italy | 1.3 | 7.4 | 26 | Reid and Brock, 2014 |

*Sorted by mass loss % due to ice cliffs
** % relative to each study area

## Figures

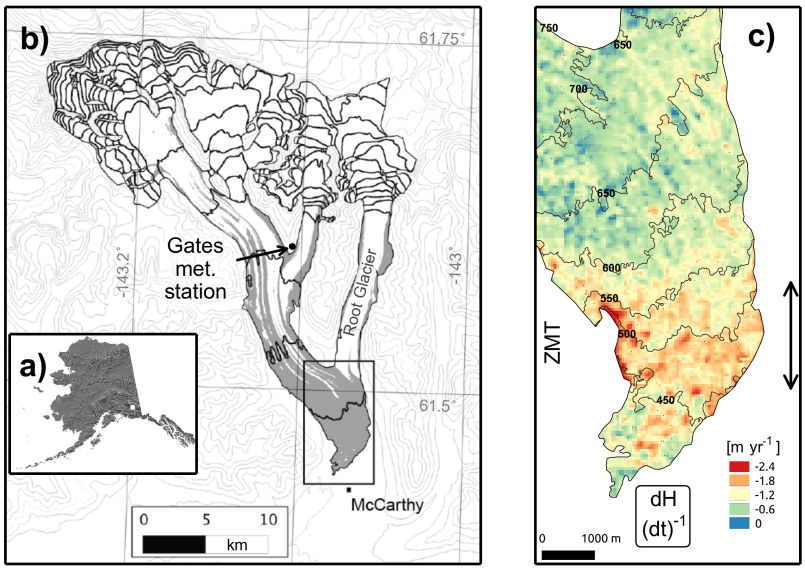


**Figure 1.** Map of Kennicott Glacier and the study area. a) Map of Alaska showing the location of panel b and the Wrangell Mountains. b) The Kennicott Glacier with the location of the Gates Glacier meteorological station (1240 m a.s.l.), discussed in the supplementary material. May Creek meteorological station is located 15 km to the southwest of McCarthy at 490 m a.s.l.. Contour intervals are 250 m based on the ASTER GDEM V2 (2009). c) Map of the general study area with dH $(dt)^{-1}$ from 1957 to 2004 see Das et al. (2014) (mean error 0.04 m $yr^{-1}$ and 1 std 0.15 m $yr^{-1}$ based on 3 $km^2$ area within 4 km of the modern terminus). *ZMT* refers to the zone of maximum thinning, the extent of which is shown with the double-headed arrow. This map of the study area includes the bare-ice parts of Root and Kennicott Glaciers, where some ablation measurements were made. Elevation contours are from 2013.

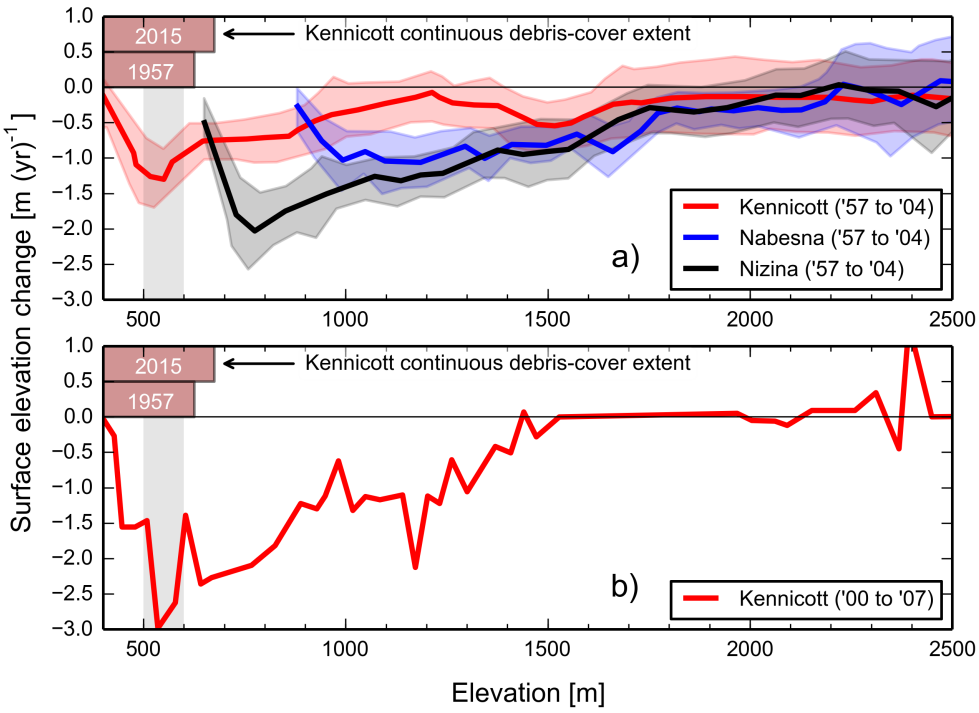


**Figure 2. Surface elevation change from three glaciers in the Wrangell mountains.** Surface elevation change data from Das et al. (2014). Elevations on the x-axis are derived from the 1957 digital elevation model (DEM). Take care in comparing these data to those presented in other figures as they are referenced to the 2013 glacier surface. a) Surface elevation change derived from the difference between DEMs. The shaded areas reflect the standard deviation of DEM differencing (see Das et al., 2014). The Kennicott Glacier is the only glacier in the figure with a continuous debris-cover spanning its entire width. The Nabesna and Nizina glaciers have individual medial moraines at the terminus but the majority of the glaciers' termini are debris-free. The vertical grey bar is the zone of maximum thinning corrected for elevation differences. The greatest change in glacier surface elevation occurs within the portion of the glacier where debris spans the glacier width continuously between 1957 and 2015 (shown as brown bars; see Supplemental Figure 26). The *ZMT* remains in a consistent location between 1957 and 2000 as well (Das et al., 2014). b) Surface elevation change derived from laser altimetry profiles differenced from a DEM from 2000 to 2007. See Das et al. (2014) for the laser altimetry path and a discussion of uncertainties.

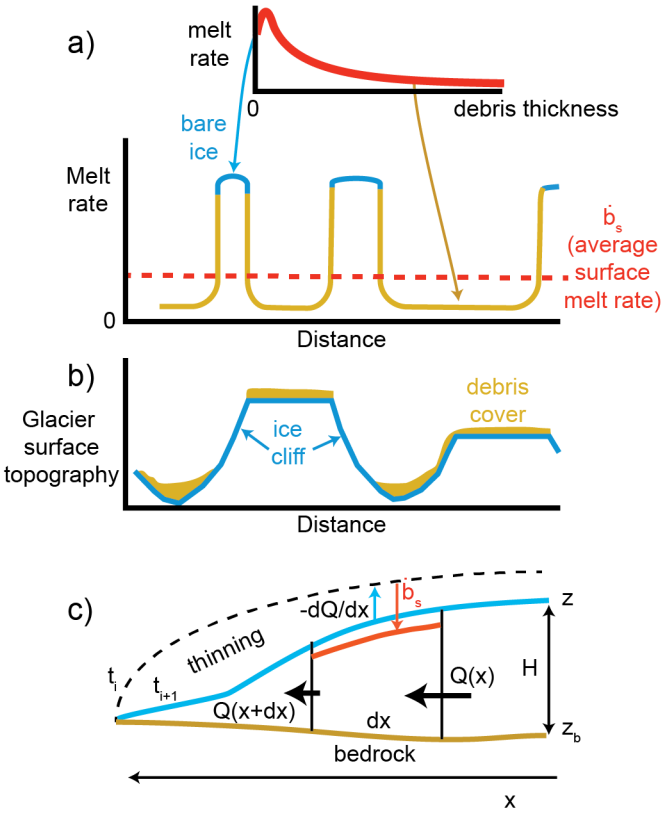


**Figure 3. Schematic comparing the relative roles of ice cliff backwasting, sub-debris melt, and ice surface uplift (ice emergence rate) to the lowering of an idealized glacier terminus.** a) Idealized relationship between ice cliff backwasting and sub-debris melt. Noting that the inclined facing and low albedo of ice cliffs can lead to melt rates that exceed bare-ice melt rates on a flat surface. b) Glacier surface topography with debris cover and ice cliffs compared to melt rates in panel a. c) Schematic showing the relationship between surface melt, ice dynamics, and the thinning of the glacier through time.

650

655

660

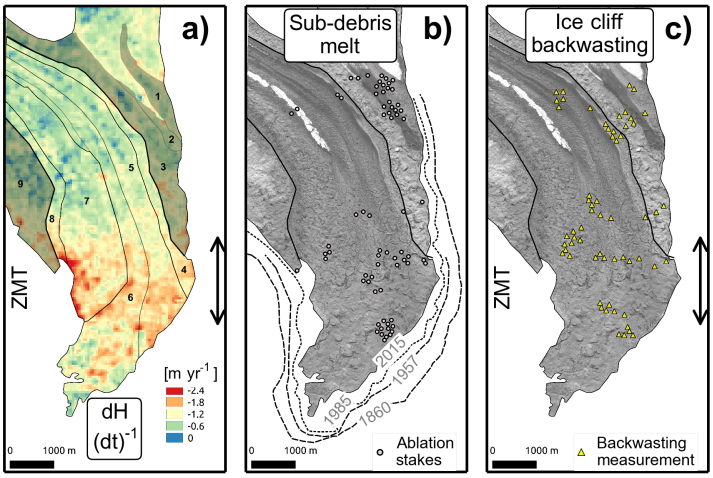


**Figure 4. The study area with defined medial moraines and in situ measurement locations.** This map of the study area includes the bare ice parts of Root Glacier, which are excluded and masked when making distributed melt estimates in which we use the area defined by the 9 medial moraines. a) dH $(dt)^{-1}$ from 1957 to 2004 see Das et al. (2014). Same thinning data as in Fig. 1C but with 9 distinct medial moraines defined and labeled. The shaded medial moraines are treated differently for distributed debris thickness estimates (see Section 2.3). Note that medial moraines # 4 through 8 contain the majority of the zone of maximum thinning. Medial moraines # 3 and 9 show much thicker debris at the same elevation than the others (Supplementary Material). The labeled and delineated moraines define the extent of the area (24.2 $km^2$) used for the distributed melt estimates described below. The zone of maximum thinning (*ZMT*) is shown by the double-headed arrow. b) Sub-debris melt rate measurement locations. Debris was measured at all locations in panels b and c, in some cases ice cliffs and sub-debris measurements were proximal and only one debris thickness measurement was made between them. The five central medial moraines are within the two black lines, within which 69% of debris thickness measurements were made. c) Locations where ice cliff backwasting was measured.

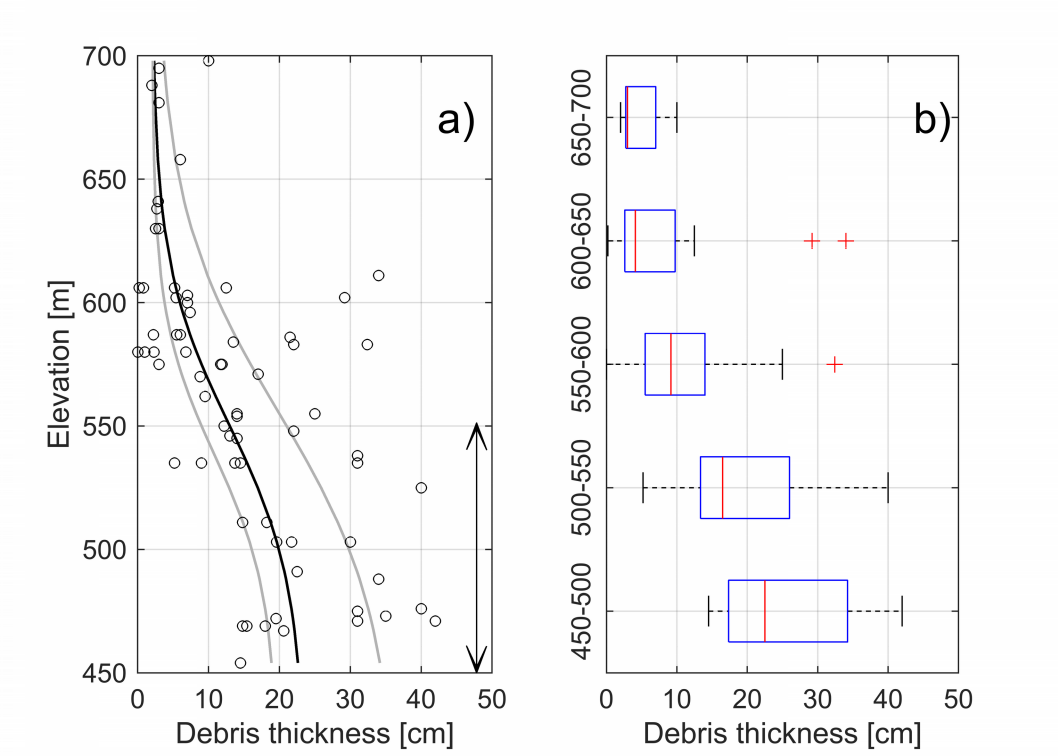


**Figure 5. Debris thickness measurements for the five central medial moraines.** a) Debris thickness measurements as they vary with elevation. The points plotted are the mean measured debris thicknesses with symmetrical uncertainties around them. The mean uncertainty of the debris thickness measurements is ±0.3 cm, with a standard deviation of ±1.8 cm, and a maximum error of ±6.7 cm. Error estimates were based on repeated measurements. With curve-fits through the median debris thickness (bold line) and the 25 and 75% quartiles (grey lines) from 50-m elevation bins shown in b (see Table 1 for curve fit parameters). The double-headed arrow represents the zone of maximum thinning. b) Box plots of debris thickness binned in 50-m elevation bands. The red bars the median and the vertical blue bars are the 25 and 75% quartiles respectively. Note the sigmoidal shape of debris thickness with elevation. See the supplementary material for curve fits applied to the other medial moraines as well as linear estimates of debris thickness with elevation.

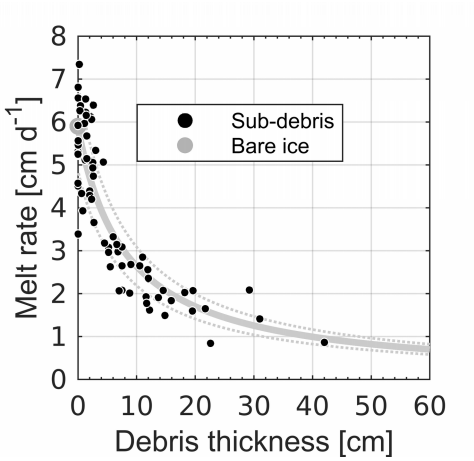


**Figure 6. Sub-debris melt rate measurements.** a) Melt rate as it varies with debris thickness. Sub-debris melt rates are corrected for the different measurement periods (Supplemental Materials). Individual melt rate measured error is smaller then the marker for each measurement, except one due to ablation pole tilt (Supplemental material). The solid line is the curve-fit using the hyper-fit model for the most likely debris thickness-melt relationship (RMSE to the data is 0.8 cm). The dotted lines represent the ±1σ error bounds used in the distributed melt estimates.

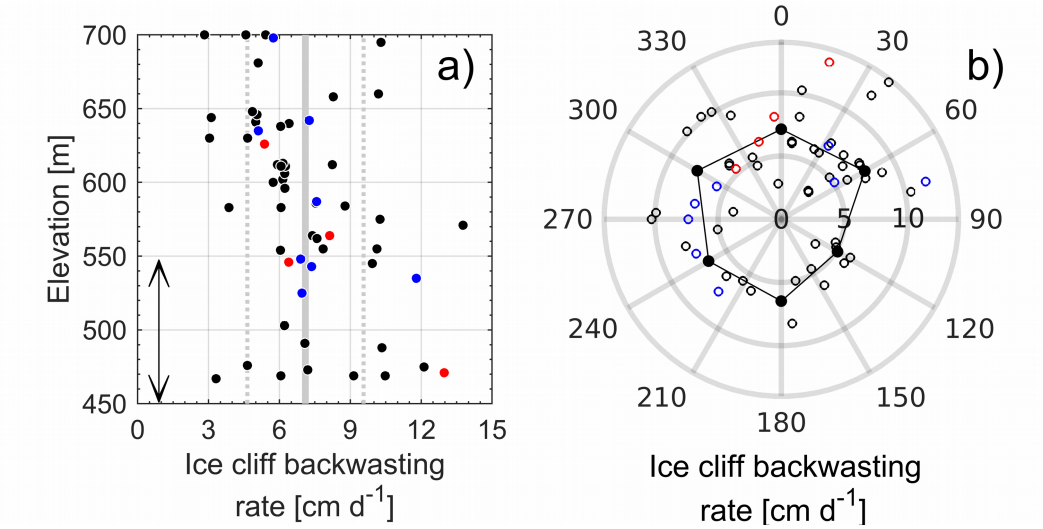


**Figure 7. Ice cliff backwasting rate measurements.** Ice cliff backwasting rates are corrected for the different measurement periods (Supplemental Materials). Cliffs with streams at their base are blue. Cliffs with ponds at their base are red. The mean error of the ice cliff backwasting rates is ±0.5 cm $d^{-1}$. Maximum error is ±1 cm $d^{-1}$ for 10 cliffs that were measured over the shortest interval of all measured ice cliffs (a three week period). The standard deviation of ice cliff backwasting errors is ±0.2 cm $d^{-1}$. a) Ice cliff backwasting rate as it varies with elevation. The solid grey line is the mean of all data 7.1 cm $d^{-1}$. The dashed lines are ±1σ bounds used in the distributed melt calculations (see Table 1 for curve fit parameters). The double-headed arrow represents the zone of maximum thinning (*ZMT*). b) Ice cliff backwasting rate as it varies with aspect. The solid black markers represent the mean backwasting rate from 60° bins. During the field survey, ice cliffs with ponds at their base were only found to face between 300 and 60 degrees (northward).

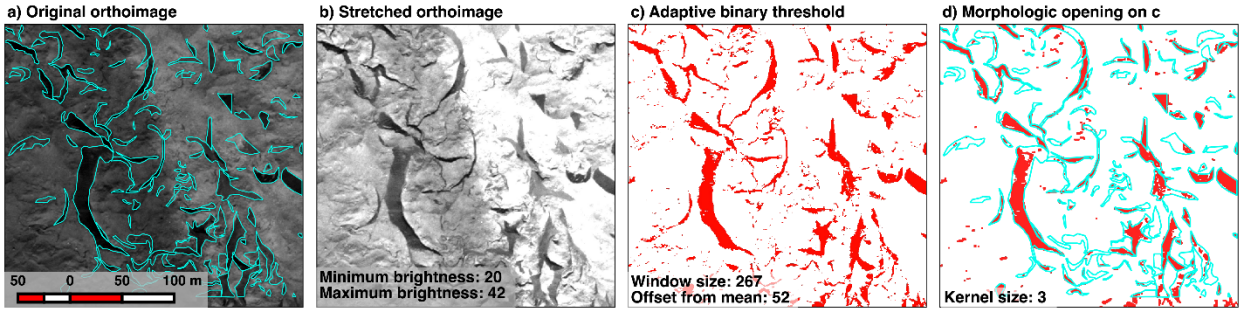


**Figure 8. Ice cliff delineation workflow for the adaptive binary threshold (*ABT*) method.** The extent of this area is shown by the third cyan box from the right in Figure 9. a) Original orthoimage with manually digitized ice cliffs shown in cyan. b) Orthoimage after histogram stretch using a set of well-performing brightness values from the parameter optimization. c) *ABT* on stretched orthoimage. d) Morphologic opening on adaptive binary threshold to remove small isolated false positive ice cliff delineations. Manually digitized ice cliffs used as the validation dataset are again shown in cyan.

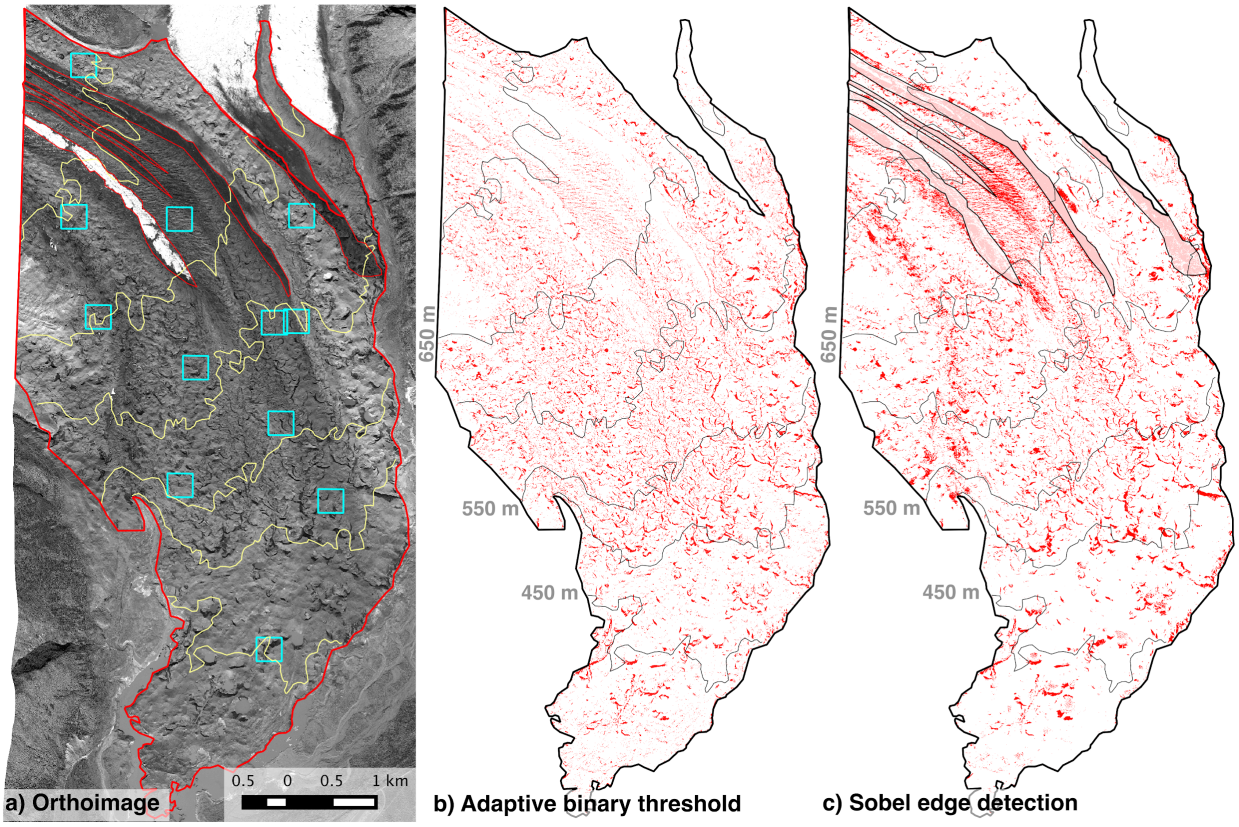


**Figure 9. Results from the two ice cliff delineation methods.** a) Orthoimage of the terminus of Kennicott Glacier, with the debris-covered area used for distributed melt estimates outlined by the thick red line. The thin red lines show regions of dark and light bare ice that required special treatment in the *SED* method. Thin yellow lines are elevation contours with a 50 m contour interval from 2013. Blue boxes show the locations of manually digitized ice cliff area, used for error analysis and parameter optimization. b) Ice cliff spatial distribution as estimated by the adaptive binary threshold (*ABT*) method, with overlaid elevation contours from 2013. The outline in panels a and b show the area used for distributed melt calculations. c) Ice cliff spatial distribution as estimated by the Sobel edge delineation (*SED*) method, with overlaid elevation contours from 2013.

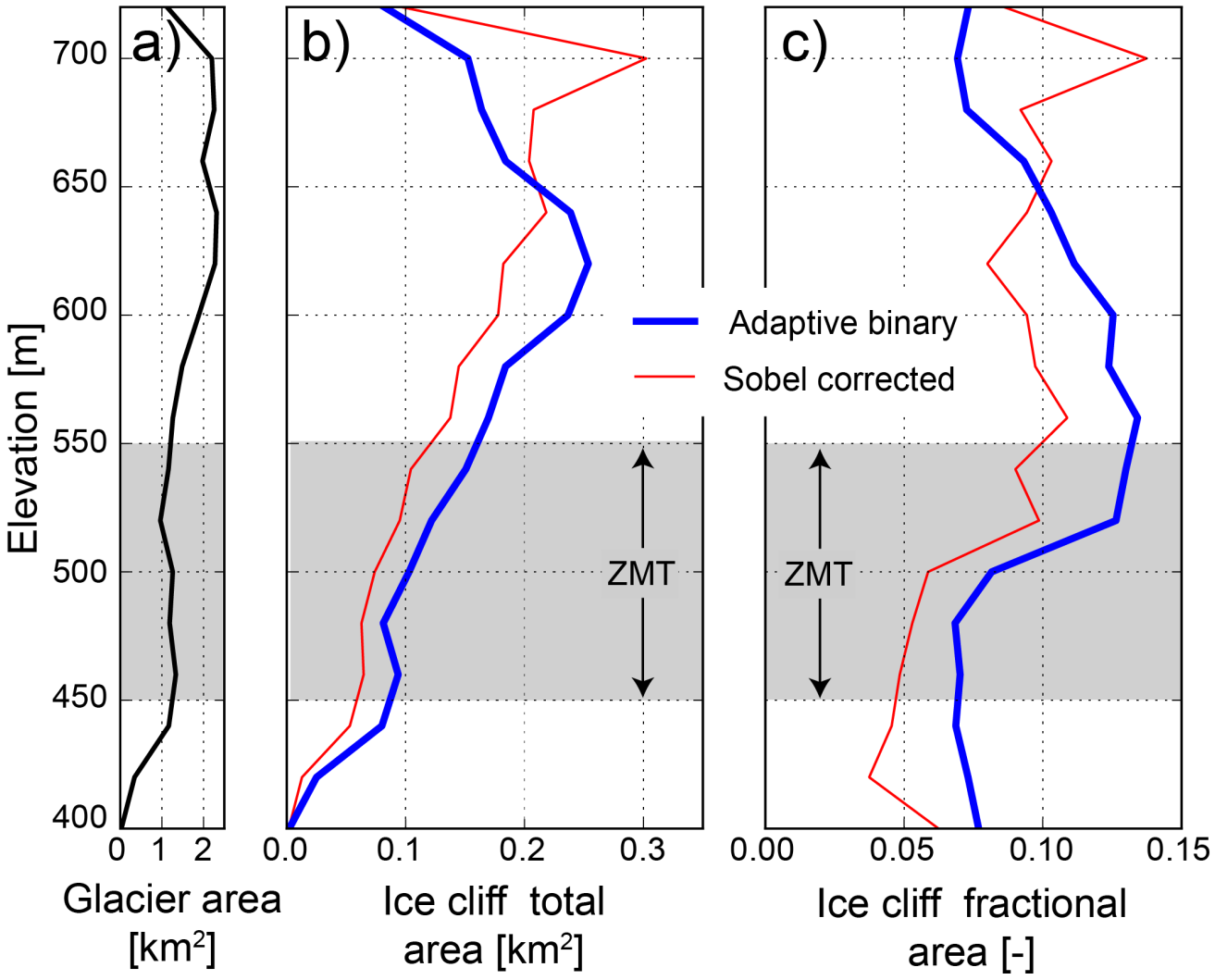


710 **Figure 10. Results from the two ice cliff delineation methods with elevation.** a) Glacier area as a function of elevation. b) Ice cliff area as a function of elevation. The red line shows results from the *SED* approach after false positives on dark colored ice are removed. c) Ice cliff area as a function of elevation, normalized by the glacier area within each elevation band. Note that fractional area * 100 is the percentage of ice cliff coverage.

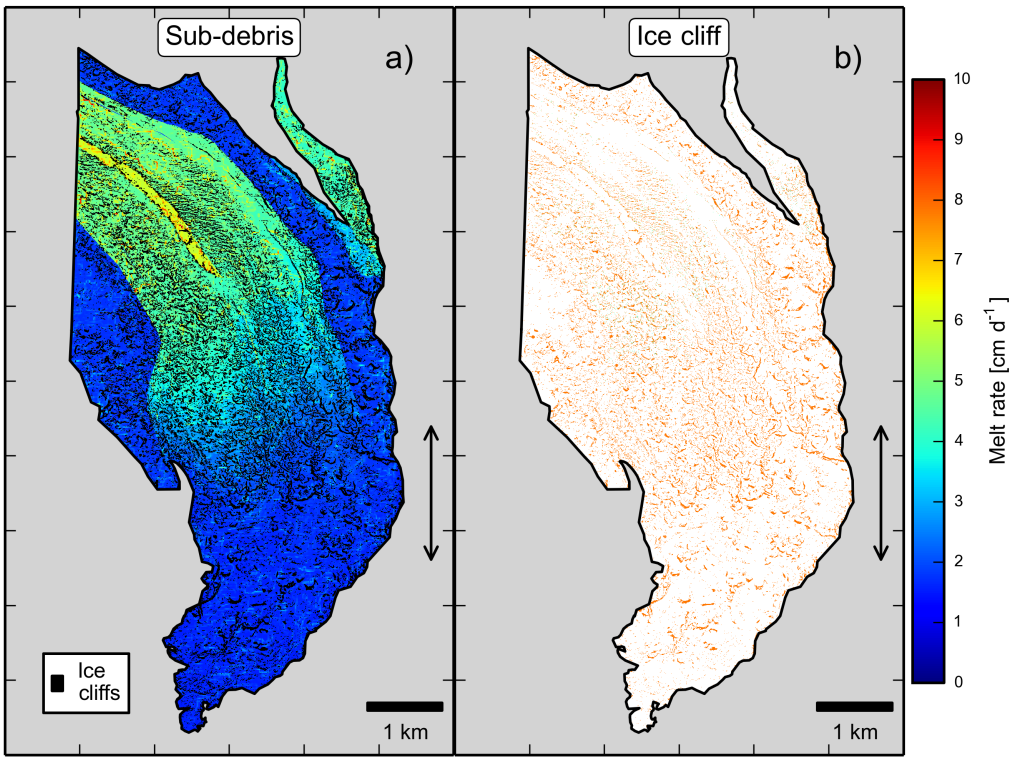


**Figure 11. Distributed melt rates based on elevation and flow path (medial moraines).** The zone of maximum thinning (*ZMT*) is defined by the double-headed arrows in each panel. a) Best sub-debris melt rate estimate which decreases in magnitude downglacier in the central part of the glacier. Medial moraines near the edge of Kennicott Glacier were composed of thicker debris. b) Most-likely ice cliff backwasting rate which we assume is uniformly distributed across the study area with a value of 7.1 cm $d^{-1}$ (see Supplementary Material for the case of backwasting rate varying linearly with elevation). Note that no clear trends were present in ice cliff backwasting rate from medial moraine to medial moraine so the same backwasting-elevation relationship is applied across the study area (Supplementary Figure 9).

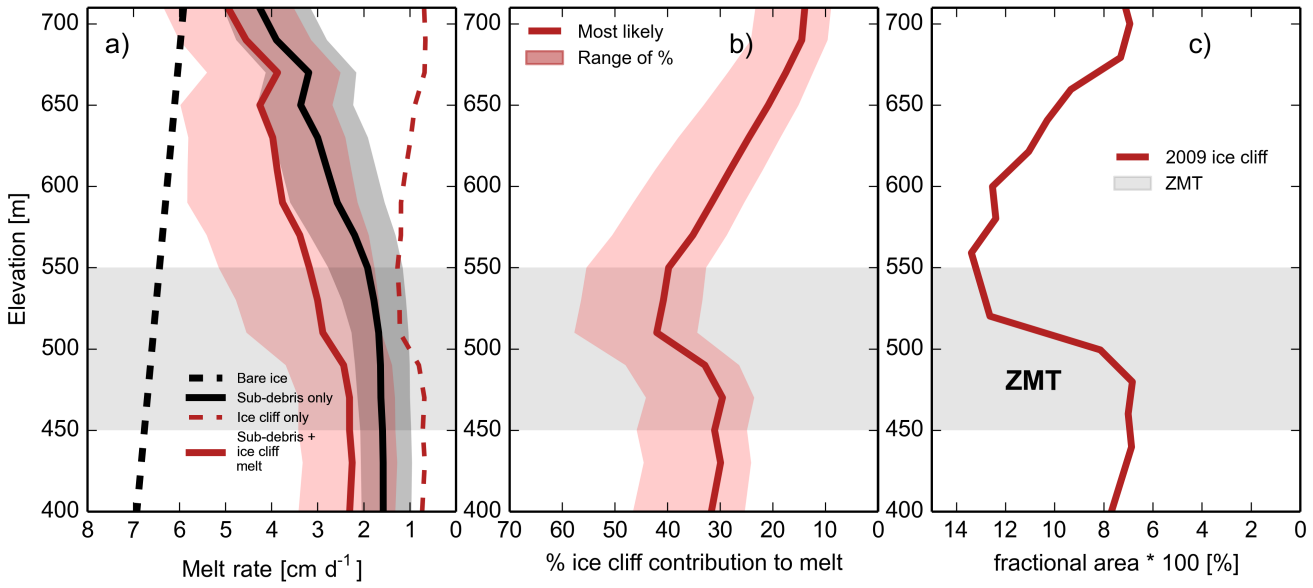


**Figure 12. Distributed melt rate estimates with elevation.** Elevations are relative to the 2013 glacier surface. The zone of maximum thinning (*ZMT*) is represented by the grey bands for all panels. a) The elevation-band-averaged melt over the study period combining in situ measurements of ice cliff, sub-debris melt, and debris thickness. The red bad contains an extreme range of sub-debris plus ice cliff melt based on compounding parameter choices such that 98.4 % of estimates lie within it (see section 2.3.1). 84.1% of estimate for sub-debris melt are within the grey shaded band. Four additional distributed melt rate scenarios are presented in the Supplementary Materials, and even with extreme parameter choices to increase melt rates, none of them maximize melt rates in the *ZMT*. Bare-ice estimates are based on the near-surface air temperature lapse rate from off-glacier meteorological stations and degree-day factor for bare-ice melt (Supplementary Materials). The decrease in sub-debris melt rate at 670 m a.s.l. is related to the increased area of medial moraine # 9 within the study area, which is covered with relatively thick debris. b) The fractional contribution of ice cliffs to the area-averaged melt rate (sub-debris + ice cliff) with elevation. The red band contains the extreme range of melt contributions from ice cliffs. c) The fractional area * 100% (percent) coverage of ice cliffs. Note that the fractional area of ice cliff coverage maximizes in the upper portion of the *ZMT*.

720